Article

Bipolar impact and phasing of Heinrich-type climate variability

https://doi.org/10.1038/s41586-023-05875-2

Received: 22 July 2022

Accepted: 9 February 2023

Published online: 24 April 2023

Check for updates

Kaden C. Martin[1✉], Christo Buizert[1], Jon S. Edwards[1], Michael L. Kalk[1], Ben Riddell-Young[1], Edward J. Brook[1], Ross Beaudette[2], Jeffrey P. Severinghaus[2] & Todd A. Sowers[3]

During the last ice age, the Laurentide Ice Sheet exhibited extreme iceberg discharge events that are recorded in North Atlantic sediments[1]. These Heinrich events have far-reaching climate impacts, including widespread disruptions to hydrological and biogeochemical cycles[2–4]. They occurred during Heinrich stadials—cold periods with strongly weakened Atlantic overturning circulation[5–7]. Heinrich-type variability is not distinctive in Greenland water isotope ratios, a well-dated site temperature proxy[8], complicating efforts to assess their regional climate impact and phasing against Antarctic climate change. Here we show that Heinrich events have no detectable temperature impact on Greenland and cooling occurs at the onset of several Heinrich stadials, and that both types of Heinrich variability have a distinct imprint on Antarctic climate. Antarctic ice cores show accelerated warming that is synchronous with increases in methane during Heinrich events, suggesting an atmospheric teleconnection[9], despite the absence of a Greenland climate signal. Greenland ice-core nitrogen stable isotope ratios, a sensitive temperature proxy, indicate an abrupt cooling of about three degrees Celsius at the onset of Heinrich Stadial 1 (17.8 thousand years before present, where present is defined as 1950). Antarctic warming lags this cooling by 133 ± 93 years, consistent with an oceanic teleconnection. Paradoxically, proximal sites are less affected by Heinrich events than remote sites, suggesting spatially complex event dynamics.

The last glacial period is characterized by the Dansgaard–Oeschger (DO) and Heinrich modes of abrupt climate variability (Fig. 1), both of which are associated with changes in the Atlantic Meridional Overturning Circulation (AMOC)[7]. The DO mode consists of alternating cold (stadial) and warm (interstadial) periods separated by decadal-scale warming transitions upwards of 10 °C in central Greenland[8]. Following the thermal bipolar seesaw theory, Antarctic climate warms during Greenland stadials and cools during interstadials[10].

Heinrich events (HEs), identified via layers of ice-rafted debris in North Atlantic marine sediments, represent short-lived, centennial-scale surges of icebergs from the Hudson Strait[1]. These HEs occur within longer, millennial-scale Heinrich stadials (HSs), which are commonly defined as periods with strong North Atlantic surface cooling and weakened AMOC strength in which an HE occurs[11,12]. HSs are further characterized by strongly weakened East Asian Monsoon (EAM) strength and enhanced dust concentrations in Greenland ice[13] (Extended Data Fig. 1, Extended Data Table 1 and Methods). The HSs do not necessarily span the full duration of the DO stadial that contains them. In each case, the HS onset precedes the HE[6], consistent with the hypothesis that the HS onset may actually trigger the HE via subsurface ocean warming during AMOC weakening[14–16].

This sequence of events is most clearly documented for the most recent Heinrich episode that occurs within DO Stadial 2 (22.9 kyr bp to 14.7 kyr bp), with HS1 starting around 17.8 kyr bp and HE1 occurring around 16.2 kyr bp (Extended Data Fig. 2). As with HS1, during HS2a and HS2b, the HS criteria are met for a subperiod of their respective DO stadials, providing the opportunity to assess HS onset phasing distinct from DO stadial onsets (Extended Data Fig. 1). For HS3–HS5, the onset of HS conditions cannot be distinguished from the onset of DO stadial conditions.

Both HEs and HSs have profound impacts on tropical hydrology, with North Atlantic cooling driving a southwards displacement of the Intertropical Convergence Zone (ITCZ)[10]. A previous study observed an abrupt methane (CH_4) increase within each HS (excluding HS3) and argued that these are caused by the HEs themselves via an extremely southwards displacement of the ITCZ[17]. For HE1 (16.2 kyr bp), the CH_4 pulse indeed coincides with the timing of ice-rafted-debris deposition[11] and with an extreme southwards displacement of the ITCZ[18,19], corroborating this idea (Extended Data Fig. 2). For earlier HEs, data of similar quality are not available. We assume that the argument in ref. 17 likewise holds for those events, and utilize their CH_4 signal as an ice-core indicator for HE timing (Extended Data Table 1).

Greenland water isotope records ($\delta^{18}O$) do not record HE features, and HSs cannot be clearly distinguished from DO stadials, possibly because their enhanced cooling signal is masked by a shift in precipitation seasonality towards summer[20]. Historically, the superb age control of ice cores enabled characterization of the bipolar phasing of Greenland and Antarctic climate during the DO cycle; the absence of

[1]College of Earth, Ocean, and Atmospheric Sciences, Oregon State University, Corvallis, OR, USA. [2]Scripps Institution of Oceanography, University of California, San Diego, CA, USA. [3]Department of Geosciences, Pennsylvania State University, State College, PA, USA. ✉e-mail: martkade@oregonstate.edu

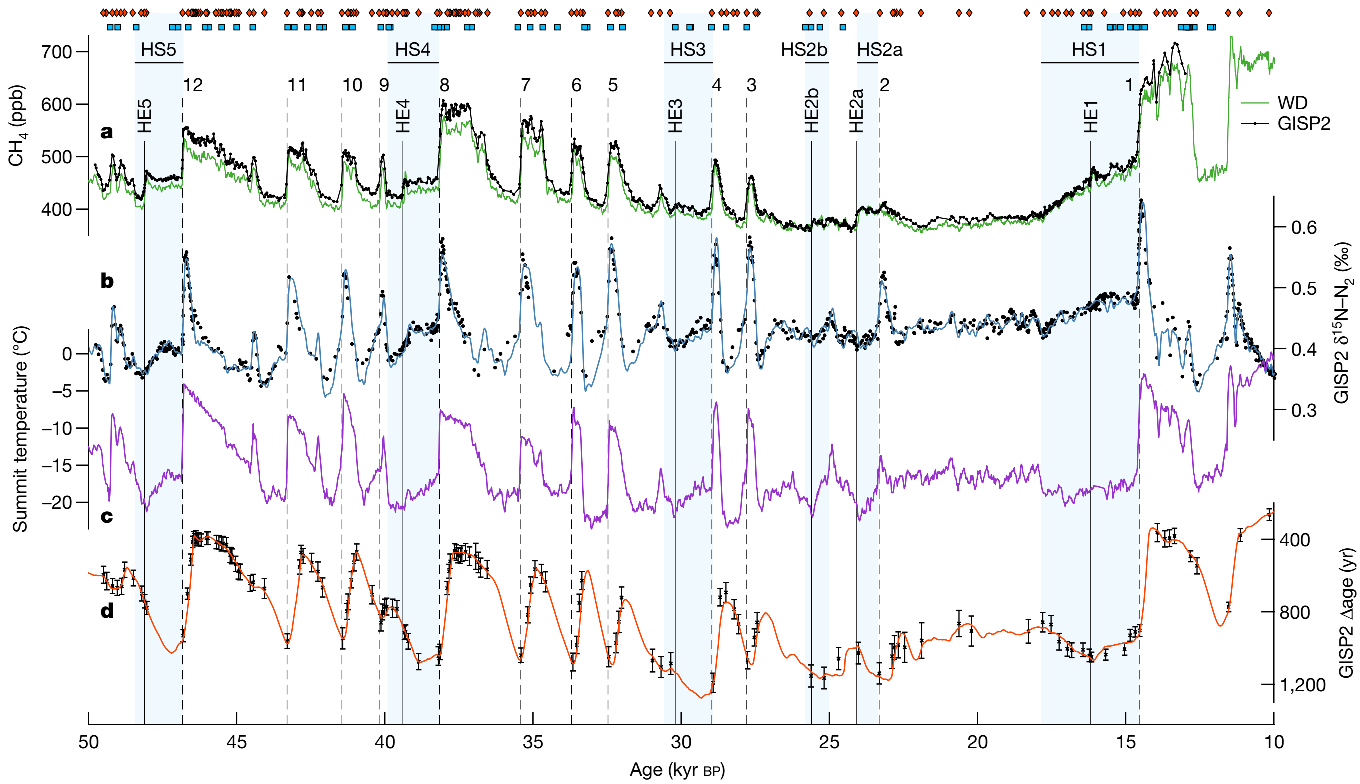

Fig. 1 | Ice-core records of Greenland climate produced in this study. a, WD CH_4 (green; ref. 17) and GISP2 CH_4 (black; this study). **b**, GISP2 $\delta^{15}N$ (model reconstruction in blue and data in black; this study). **c**, GISP2 temperature anomaly reconstruction (purple; this study, estimated 2σ uncertainty of 2.2 °C). **d**, GISP2 Δage (model reconstruction in orange and data and 2σ uncertainty (Methods) in black, note the inverted scale; this study). The light blue vertical bars denote Heinrich stadials. The solid and dashed vertical lines indicate the timing of HEs and DO warming transitions, respectively, inferred by the midpoint of CH_4 features. The red diamonds indicate CH_4 (gas phase) matchpoints between WD and GISP2 and the blue squares indicate volcanic (ice phase) matchpoints between WD and GISP2 (ref. 27).

a significantly pronounced Greenland $\delta^{18}O$ signal precludes the same analysis for Heinrich-type variability. As strong Antarctic climate shifts during HSs have no corresponding change in Greenland, it has been suggested that the bipolar seesaw breaks down during these periods[21]. Here we utilize an alternative temperature proxy to investigate the impacts of HEs and HSs on Greenland climate, and to assess their phasing with Antarctic climate.

Updated Greenland climate records

We present high-resolution records of the isotopic ratio of ^{15}N to ^{14}N in N_2 ($\delta^{15}N–N_2$) and of atmospheric CH_4 mixing ratios from the Greenland Ice Sheet Project 2 (GISP2) ice core (Fig. 1). The $\delta^{15}N$ is well established as a sensitive and seasonally unbiased recorder of abrupt climate change[22]. Surface temperature changes produce thermal gradients between the snow surface and the gas lock-in depth 60–80 m below the surface, imparting transient isotopic $\delta^{15}N$ excursions proportional to the size of the temperature change. Temperature reconstructions using the $\delta^{15}N$ method have previously been applied to the DO cycle, but not to Heinrich variability. Compared with previous work, our $\delta^{15}N$ record provides about an order of magnitude better precision (0.0025‰) and up to 3 times increased time resolution around HEs.

The CH_4 record has a median age resolution of 32 yr from 50 kyr BP to 10 kyr BP, and is corrected for in situ production of CH_4 during analysis[23]. We identify centennial-scale variability common to the West Antarctic Ice Sheet Divide (WD) ice core[17] and GISP2 CH_4 records, allowing for the synchronization of their gas-age scales[24–26] via 151 stratigraphic tie points (Fig. 1). Recently identified interhemispheric volcanic tie points[27] allow for the synchronization of their ice-age scales (Extended Data Fig. 3). With both gas and ice phases independently synchronized, the GISP2 Δage (the gas-age–ice-age difference) can be estimated empirically (Fig. 1) as WD Δage is relatively small, stable and well characterized (Methods). The Δage is sensitive to temperature, providing an additional climate proxy[28].

We utilize an inverse firn model[24,29] to reconstruct past temperature and accumulation changes associated with Heinrich variability at the site (Fig. 1). We advance previous firn model studies[30] through high-resolution and high-precision measurements of $\delta^{15}N$, and through empirical Δage constraints. This methodology provides accurate surface temperature reconstructions, as it is not subject to temporal variability in the $\delta^{18}O$–temperature relationship.

Greenland signature of Heinrich events

We identify no abrupt transient features in $\delta^{15}N$ during HEs, indicating that these events have no temperature impact in central Greenland. Using a series of idealized firn model experiments (Methods) centred on the HE1 abrupt CH_4 increase, we find a probable upper bound of 1 °C cooling over 125 yr for the Greenland climate response (Extended Data Fig. 4). This is well within the background temperature variability at the site[31], and therefore we deem it insignificant. This observation is in contrast to climate modelling studies that typically simulate HEs as extended periods of strong Greenland cooling[32,33].

Minor HE depletions in Greenland Summit (average of the Greenland Ice Core Project (GRIP) and GISP2 cores) $\delta^{18}O$ are synchronous with abrupt CH_4 increases associated with some HEs. These are most apparent during HE1 and HE4 (Figs. 2 and 3), but not found in all Greenland cores (Extended Data Fig. 5). As there is no corresponding $\delta^{15}N$ feature, this probably reflects a short-lived variation in vapour transport or precipitation seasonality rather than a site temperature change.

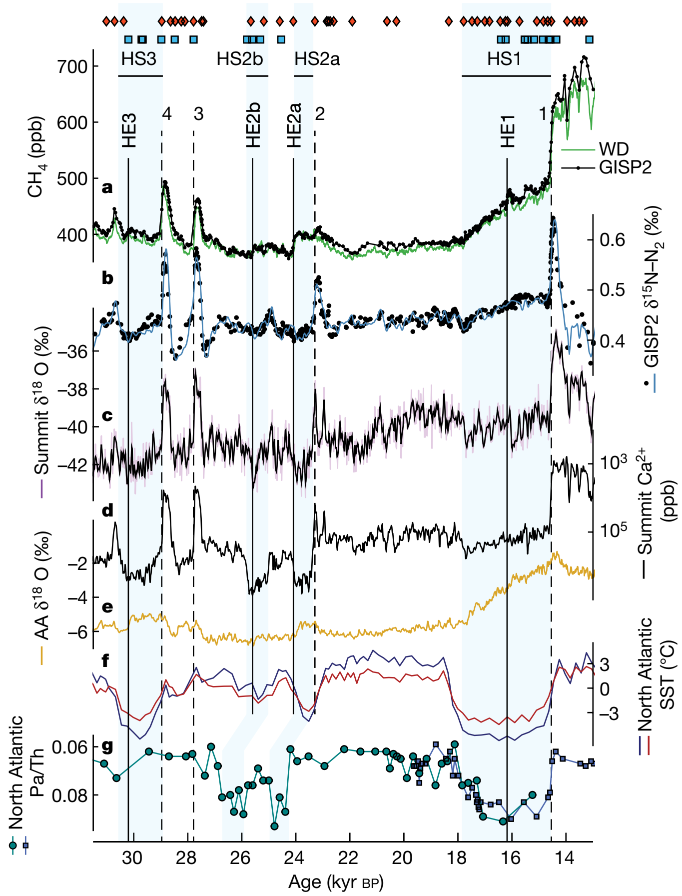

Fig. 2 | Records of millennial-scale climate variability from HS3 to HS1. **a**, WD CH_4 (green; ref. 17) and GISP2 CH_4 (black; this study). **b**, GISP2 $\delta^{15}N$ (modelled reconstruction in blue and data in black; this study). **c**, Summit $\delta^{18}O$ (GISP2 and GRIP average, purple; 100-year running average, black; ref. 48). **d**, Summit Ca^{2+} (black; ref. 38). **e**, Six-core Antarctic average (AA) $\delta^{18}O$ (gold; refs. 9,49). **f**, North Atlantic stack (dark red) and Iberian Margin (dark blue) sea surface temperature (SST) reconstruction transferred from GICC05 to the bipolar ice-core chronology used here[36]. **g**, Bermuda Rise $^{231}Pa/^{230}Th$ (blue squares[50] and teal circles[37]). The light blue bars denote HSs. It is noted that blue bars are shifted by 900 yr during HS2a and HS2b for Pa/Th records. The solid and dashed vertical lines indicate timing of HEs and DO warming transitions, respectively, inferred by the midpoint of CH_4 features. The red diamonds indicate CH_4 (gas phase) matchpoints between WD and GISP2 and the blue squares indicate volcanic (ice phase) matchpoints between WD and GISP2 (ref. 27).

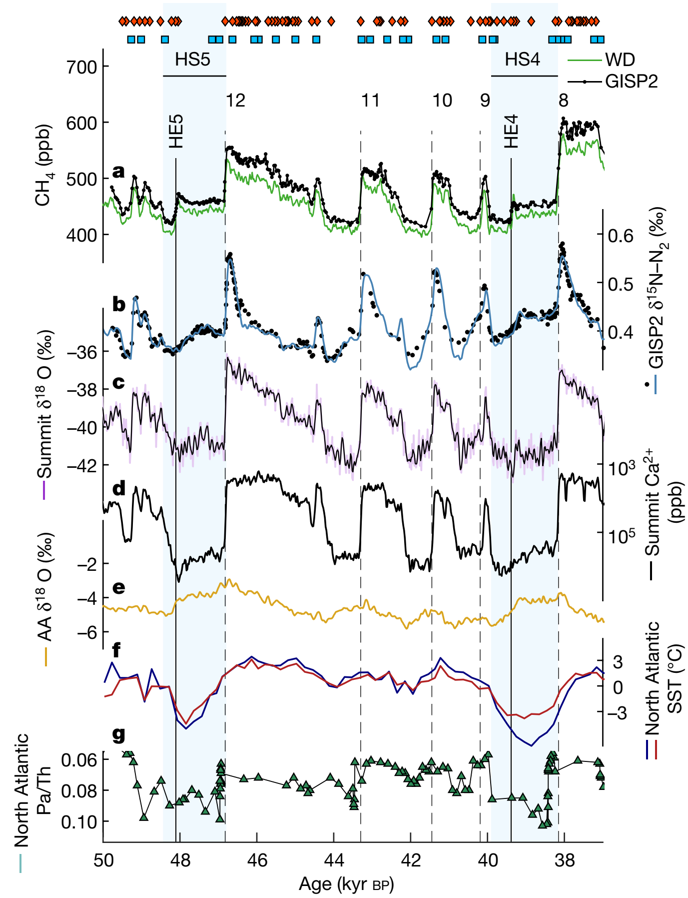

Fig. 3 | Records of millennial-scale climate variability from HS5 to HS4. **a**, WD CH_4 (green; ref. 17) and GISP2 CH_4 (black; this study). **b**, GISP2 $\delta^{15}N$ (modelled reconstruction in blue and data in black; this study). **c**, Summit $\delta^{18}O$ (GISP2 and GRIP average, purple; 100-year running average, black; ref. 48). **d**, Summit Ca^{2+} (black; ref. 38). **e**, Six-core AA $\delta^{18}O$ (gold; refs. 9,49). **f**, North Atlantic stack (dark red) and Iberian Margin (dark blue) SST reconstruction transferred from GICC05 to the bipolar ice-core chronology used here[36]. **g**, Bermuda Rise $^{231}Pa/^{230}Th$ (green triangles[5]). The vertical light blue bars denote HSs. The solid and dashed vertical lines indicate timing of HEs and DO warming transitions, respectively, inferred by the midpoint of CH_4 features. The red diamonds indicate CH_4 (gas phase) matchpoints between WD and GISP2 and the blue squares indicate volcanic (ice phase) matchpoints between WD and GISP2 (ref. 27).

Greenland signature of Heinrich stadials

At the onset of HS1 at 17.8 kyr bp, we observe a modest but abrupt depletion in $\delta^{15}N$, indicating a rapid cooling of about 3 °C that has not been recognized previously. In our reconstruction, cold conditions persist for the duration of HS1 (Fig 1). A weak HS1 onset cooling signal is visible in the Summit $\delta^{18}O$ record, but not in other Greenland $\delta^{18}O$ records (Extended Data Fig. 5). A recent $\delta^{18}O$-based data assimilation study[34] was not able to reproduce this cooling. Isotope-enabled climate model simulations suggest that HS1 onset cooling can be reconciled with a weak or even absent $\delta^{18}O$ signature by accounting for increased seasonality of Greenland precipitation[20] (Extended Data Fig. 6).

HS2 (about 26–23 kyr bp) has two distinct periods reflecting HS conditions, identified as HS2b and HS2a[35] (Fig. 2). The double structure is observed most clearly in records of sea surface temperature and faunal assemblage in the high-sedimentation Iberian Margin region[36], but is also indicated by Bermuda Rise $^{231}Pa/^{230}Th$ (refs. 5,37), increased dust deposition in Greenland[38] and EAM weakening[39]. GISP2 $\delta^{15}N$ does not capture the HS2b onset, yet Δage increases—a pattern that indicates gradual cooling. We reconstruct warming at the termination of HS2b, followed by a weak, yet abrupt, cooling at the onset of HS2a (Fig. 2). HS2a is then terminated by abrupt warming at the onset of DO Interstadial 2.

Unlike HS2b and HS1, we identify no abrupt cooling signals at onset of HS3–HS5. This implies that the HS onset is either indistinguishable in timing from the onset of their respective DO stadials or too gradual to impact $\delta^{15}N$ as with HS2b. Notably, the EAM and North Atlantic quickly reach HS conditions, with a Greenland calcium peak during early HS5. Our reconstruction suggests that temperatures reach a minimum in the early HS, followed by a gradual warming until abrupt DO warming.

The gradual warming during HSs inferred by our firn model reconstruction could be the result of increased radiative forcing due to increasing atmospheric carbon dioxide (CO_2) and CH_4 (ref. 40). The difference between the temperature trends observed in HS and DO stadial conditions may also reflect the reconstruction approach, where lower data availability in $\delta^{15}N$ and Δage during DO stadials limits the ability to resolve weak trends.

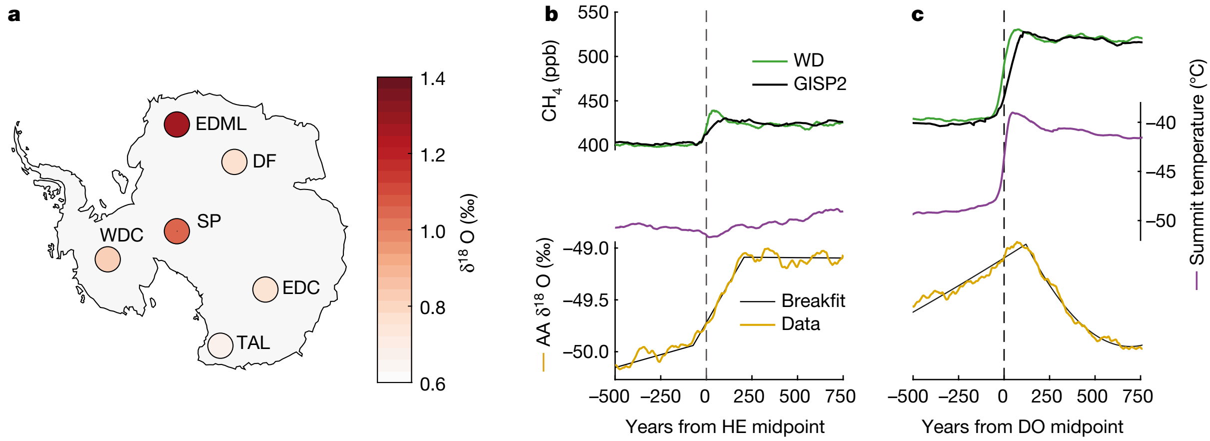

Fig. 4 | Spatial pattern of Antarctic $\delta^{18}O$ change during an HE. Stacked record of Greenland and Antarctic climate during HE and DO stadial-to-interstadial transitions. **a**, The magnitude of Antarctic $\delta^{18}O$ change during an HE. The change is defined as the difference between the pre-event (−300 yr to −50 yr) and post-event (200 yr to 450 yr) average for each site. (Sites: SP, South Pole; WDC, West Antarctic Ice Sheet Divide; EDML, EPICA Dronning Maud Land; DF, Dome Fuji; EDC, EPICA Dome C; TAL, Talos Dome). **b**, HE event stacks, from top to bottom: GISP2 (black; this study) and WD (green; ref. 17) CH_4, Summit temperature reconstruction (purple; this study) and six-core AA $\delta^{18}O$ stack (gold; refs. 9,49). Breakfit was used to identify significant changes in AA $\delta^{18}O$, and a curve was fitted between these points (black; Methods). Individual events were aligned at the midpoint of abrupt CH_4 increases then averaged. **c**, The same as in **b**, but for DO warming transitions. Individual events were aligned at the midpoint of abrupt calcium increases then averaged.

Bipolar climate phasing

We first investigate the bipolar phasing during HEs by utilizing the abrupt CH_4 increases to indicate their timing[17]. We compare bipolar climate records via a stacking procedure[9] (Fig. 4) in which individual HEs are aligned at the midpoints of abrupt CH_4 increases and averaged (Methods); for comparison, a stack of DO warming transitions is also provided.

For HEs, we identify synchronous climatic changes in the low latitudes (that is, tropical CH_4 source regions) and Antarctica. At the abrupt HE-related CH_4 increase, the gradual warming trend in Antarctic $\delta^{18}O$ abruptly accelerates (Fig. 4). Within uncertainty of interhemispheric synchronization and multi-core averaging, the acceleration of Antarctic warming occurs synchronously with, or slightly leads, the midpoint of the abrupt HE-related CH_4 increase (72 ± 76 yr; Methods). The spatial pattern of Antarctic change is heterogeneous with a stronger warming signal observed for the European Project for Ice Coring in Antarctica (EPICA) Dronning Maud Land (EDML) and the South Pole (SP) ice cores (Fig. 4a). The fast interhemispheric coupling is suggestive of an atmospheric teleconnection of the northern HE signal to the southern high latitudes, in contrast to the time-delayed oceanic coupling observed during DO warming transitions[9].

The HE stacking includes HE2a, which has an easily recognized CH_4 increase[17]. It is unclear whether HS2b also has an HE associated with it; however, we identify an abrupt CH_4 increase during a period of Summit $\delta^{18}O$ depletion and high dust deposition (Extended Data Fig. 7). The 21-ppb HS2b CH_4 signal is seen in both the WD and the GISP2 records, yet it is smaller than the average range of HE1–HE5 (37 ± 11 ppb). Although small, our analysis suggests that the HS2b abrupt CH_4 increase is likewise synchronous with Antarctic warming, suggesting that this phasing may hold even for weak events.

Next, we investigate bipolar climate phasing during HSs, which is most evident during HS1. The abrupt 3 °C HS1 onset cooling in Greenland precedes Antarctic HS1 warming by 133 ± 93 yr (Extended Data Fig. 2). As GISP2 $\delta^{15}N$ and CH_4 have no relative age uncertainty, the uncertainty in this phasing is due primarily to uncertainty in the WD Δage and in the Antarctic change-point detection.

For comparison, in the most recent estimates from bipolar volcanic synchronization[27], the Antarctic bipolar seesaw response during the DO cycle is delayed by 122 ± 24 yr behind the midpoint of Greenland abrupt DO climate transitions (Methods). The bipolar phasing we infer for the onset of HS1 is thus in good agreement with the operation of the bipolar seesaw during the DO cycle. This argues for a Northern Hemisphere driver for HS1, rather than Antarctic volcanism as proposed elsewhere[41].

Discussion

The abrupt acceleration of Antarctic warming synchronous with HEs represents a mode of climate variability not captured by the thermal bipolar seesaw model. This warming is most pronounced at EDML in the Atlantic sector, but is observed in all Antarctic cores[9] (Fig. 4a). The fast climate coupling during HEs suggests the dominance of an atmospheric teleconnection, plausibly propagated from the North Atlantic to Antarctica via the well established southwards shift of the ITCZ. This shift is probably accompanied by a similar shift of the Southern Hemisphere westerly winds[9,42]. This shift of the Southern Hemisphere westerlies may have driven the observed Antarctic warming, for example, via enhanced upwelling of warmer mid-depth waters[43], a decrease in sea ice, or increased oceanic heat transport to Antarctica via the gyre or overturning circulation[44]. The enhanced upwelling of mid-depth waters and reduced sea ice could also lead to the observed abrupt increases in atmospheric CO_2 synchronous with HE-related CH_4 increases[44,45].

Palaeoceanographic literature has long recognized the existence of three glacial AMOC modes, commonly described as strong (interstadial), weak (stadial) and off (HS)[37]. As Heinrich-type variability is not expressed in Greenland $\delta^{18}O$, the Greenland event stratigraphy recognizes only the interstadial and stadial glacial climate states[46]—limiting its usefulness in describing global climate dynamics. Our work confirms that the HSs are climatically distinct from DO stadial conditions, distinguished in Greenland by colder temperatures. Although this distinction cannot be made in the Greenland ice-core record for HS3–HS5, it meaningfully refines our understanding of HS2b, HS2a and HS1. This observation highlights that significant differences in timing and dynamics exist between the five Heinrich episodes. We find that the centennial-scale bipolar climate phasing at the HS1 onset is similar to that of the DO cycle, corroborating the involvement of the AMOC and suggesting that the bipolar seesaw is functioning normally at HS[21] onsets.

Greenland climate is strongly coupled to the North Atlantic in both observations and models, and a pronounced Greenland cooling signal is found in HE model simulations[32]. Our observations demonstrate the absence of an abrupt Greenland climate signal during HEs, indicating that far-field regions such as the tropics and southern high latitudes are more strongly impacted by HEs than near-field ones. We speculate that this proximity paradox may be the result of a mechanism outside of the North Atlantic region, possibly in the tropical Pacific[47]. Alternatively, North Atlantic sea ice extends so far south during the early HS that further expansion no longer affects Greenland temperature.

The Greenland δ^{18}O depletions associated with some HEs and HSs appear dependent on the location of the record, as Summit captures them but the North Greenland Eemian Ice Drilling Project (NEEM) and North Greenland Ice Core Project (NGRIP) ice cores do not. Combining these temperature reconstructions with existing water isotope data may inform us about hydrological changes around Greenland. Our work provides insight into the Greenland climate impacts of Heinrich-type variability, valuable benchmarks for climate models, and an expanded understanding of bipolar climate coupling during the last glacial period.

Online content

Any methods, additional references, Nature Portfolio reporting summaries, source data, extended data, supplementary information, acknowledgements, peer review information; details of author contributions and competing interests; and statements of data and code availability are available at https://doi.org/10.1038/s41586-023-05875-2.

1. Hemming, S. R. Heinrich events: massive late Pleistocene detritus layers of the North Atlantic and their global climate imprint. *Rev. Geophys.* **42**, RG1005 (2004).
2. Bauska, T. K. et al. Carbon isotopes characterize rapid changes in atmospheric carbon dioxide during the last deglaciation. *Proc. Natl Acad. Sci. USA* **113**, 3465–3470 (2016).
3. Strikis, N. M. et al. South American monsoon response to iceberg discharge in the North Atlantic. *Proc. Natl Acad. Sci. USA* **115**, 3788–3793 (2018).
4. Nguyen, D. C. et al. Precipitation response to Heinrich Event-3 in the northern Indochina as revealed in a high-resolution speleothem record. *J. Asian Earth Sci. X* **7**, 100090 (2022).
5. Henry, L. G. et al. North Atlantic ocean circulation and abrupt climate change during the last glaciation. *Science* **353**, 470–474 (2016).
6. Barker, S. et al. Icebergs not the trigger for North Atlantic cold events. *Nature* **520**, 333–336 (2015).
7. Lynch-Stieglitz, J. The Atlantic Meridional Overturning Circulation and abrupt climate change. *Ann. Rev. Mar. Sci.* **9**, 83–104 (2017).
8. Capron, E. et al. The anatomy of past abrupt warmings recorded in Greenland ice. *Nat. Commun.* **12**, 2106 (2021).
9. Buizert, C. et al. Abrupt ice-age shifts in southern westerly winds and Antarctic climate forced from the north. *Nature* **563**, 681–685 (2018).
10. Pedro, J. B. et al. Beyond the bipolar seesaw: toward a process understanding of interhemispheric coupling. *Quat. Sci. Rev.* **192**, 27–46 (2018).
11. Hodell, D. A. et al. Anatomy of Heinrich Layer 1 and its role in the last deglaciation. *Paleoceanography* **32**, 284–303 (2017).
12. Barker, S. et al. Interhemispheric Atlantic seesaw response during the last deglaciation. *Nature* **457**, 1097–1102 (2009).
13. Dong, X. et al. Coupled atmosphere–ice–ocean dynamics during Heinrich Stadial 2. *Nat. Commun.* **13**, 5867 (2022).
14. Marcott, S. A. et al. Ice-shelf collapse from subsurface warming as a trigger for Heinrich events. *Proc. Natl Acad. Sci. USA* **108**, 13415–13419 (2011).
15. Max, L., Nürnberg, D., Chiessi, C. M., Lenz, M. M. & Mulitza, S. Subsurface ocean warming preceded Heinrich events. *Nat. Commun.* **13**, 4217 (2022).
16. Yang, X., Rial, J. A. & Reischmann, E. P. On the bipolar origin of Heinrich events. *Geophys. Res. Lett.* **41**, 9080–9086 (2014).
17. Rhodes, R. H. et al. Enhanced tropical methane production in response to iceberg discharge in the North Atlantic. *Science* **348**, 1016–1019 (2015).
18. Cheng, H., Sinha, A., Wang, X., Cruz, F. W. & Edwards, R. L. The Global Paleomonsoon as seen through speleothem records from Asia and the Americas. *Clim. Dyn.* **39**, 1045–1062 (2012).
19. Deplazes, G. et al. Links between tropical rainfall and North Atlantic climate during the last glacial period. *Nat. Geosci.* **6**, 213–217 (2013).
20. He, C. et al. Abrupt Heinrich Stadial 1 cooling missing in Greenland oxygen isotopes. *Sci. Adv.* **7**, eabh1007 (2021).
21. Landais, A. et al. A review of the bipolar see-saw from synchronized and high resolution ice core water stable isotope records from Greenland and East Antarctica. *Quat. Sci. Rev.* **114**, 18–32 (2015).
22. Severinghaus, J. P., Sowers, T., Brook, E. J., Alley, R. B. & Bender, M. L. Timing of abrupt climate change at the end of the Younger Dryas interval from thermally fractionated gases in polar ice. *Nature* **391**, 141–146 (1998).
23. Lee, J. E. et al. Excess methane in Greenland ice cores associated with high dust concentrations. *Geochim. Cosmochim. Acta* **270**, 409–430 (2020).
24. Buizert, C. et al. The WAIS Divide deep ice core WD2014 chronology—Part 1: methane synchronization (68–31 ka bp) and the gas age–ice age difference. *Clim. Past* **11**, 153–173 (2015).
25. Sigl, M. et al. The WAIS Divide deep ice core WD2014 chronology—Part 2: annual-layer counting (0–31 ka bp). *Clim. Past* **12**, 769–786 (2016).
26. Seierstad, I. K. et al. Consistently dated records from the Greenland GRIP, GISP2 and NGRIP ice cores for the past 104ka reveal regional millennial-scale δ^{18}O gradients with possible Heinrich event imprint. *Quat. Sci. Rev.* **106**, 29–46 (2014).
27. Svensson, A. et al. Bipolar volcanic synchronization of abrupt climate change in Greenland and Antarctic ice cores during the last glacial period. *Clim. Past* **16**, 1565–1580 (2020).
28. Buizert, C. The ice core gas age–ice age difference as a proxy for surface temperature. *Geophys. Res. Lett.* **48**, e2021GL094241 (2021).
29. Buizert, C. et al. Antarctic surface temperature and elevation during the Last Glacial Maximum. *Science* **372**, 1097–1101 (2021).
30. Kindler, P. et al. Temperature reconstruction from 10 to 120 kyr b2k from the NGRIP ice core. *Clim. Past* **10**, 887–902 (2014).
31. Kobashi, T. et al. High variability of Greenland surface temperature over the past 4000 years estimated from trapped air in an ice core. *Geophys. Res. Lett.* **38**, 4–9 (2011).
32. Menviel, L. C., Skinner, L. C., Tarasov, L. & Tzedakis, P. C. An ice–climate oscillatory framework for Dansgaard–Oeschger cycles. *Nat. Rev. Earth Environ.* **1**, 677–693 (2020).
33. Ziemen, F. A., Kapsch, M. L., Klockmann, M. & Mikolajewicz, U. Heinrich events show two-stage climate response in transient glacial simulations. *Clim. Past* **15**, 153–168 (2019).
34. Badgeley, J. A., Steig, E. J., Hakim, G. J. & Fudge, T. J. Greenland temperature and precipitation over the last 20000 years using data assimilation. *Clim. Past* **16**, 1325–1346 (2020).
35. Bard, E., Rostek, F., Turon, J. L. & Gendreau, S. Hydrological impact of Heinrich events in the subtropical northeast Atlantic. *Science* **289**, 1321–1324 (2000).
36. Pedro, J. B. et al. Dansgaard–Oeschger and Heinrich event temperature anomalies in the North Atlantic set by sea ice, frontal position and thermocline structure. *Quat. Sci. Rev.* **289**, 107599 (2022).
37. Böhm, E. et al. Strong and deep Atlantic meridional overturning circulation during the last glacial cycle. *Nature* **517**, 73–76 (2015).
38. Mayewski, P. A. et al. Major features and forcing of high-latitude Northern Hemisphere atmospheric circulation using a 110,000-year-long glaciochemical series. *J. Geophys. Res. Ocean* **102**, 26345–26366 (1997).
39. Cheng, H. et al. The Asian monsoon over the past 640,000 years and ice age terminations. *Nature* **534**, 640–646 (2016).
40. Bauska, T. K., Marcott, S. A. & Brook, E. J. Abrupt changes in the global carbon cycle during the last glacial period. *Nat. Geosci.* **14**, 91–96 (2021).
41. McConnell, J. R. et al. Synchronous volcanic eruptions and abrupt climate change ~17.7 ka plausibly linked by stratospheric ozone depletion. *Proc. Natl Acad. Sci. USA* **114**, 10035–10040 (2017).
42. Ceppi, P., Hwang, Y. T., Liu, X., Frierson, D. M. W. & Hartmann, D. L. The relationship between the ITCZ and the Southern Hemispheric eddy-driven jet. *J. Geophys. Res. Atmos.* **118**, 5136–5146 (2013).
43. Ferrari, R. et al. Antarctic sea ice control on ocean circulation in present and glacial climates. *Proc. Natl Acad. Sci. USA* **111**, 8753–8758 (2014).
44. Menviel, L. et al. Southern Hemisphere westerlies as a driver of the early deglacial atmospheric CO_2 rise. *Nat. Commun.* **9**, 2503 (2018).
45. Menviel, L., England, M. H., Meissner, K. J., Mouchet, A. & Yu, J. Atlantic–Pacific seesaw and its role in outgassing CO_2 during Heinrich events. *Paleoceanography* **29**, 58–70 (2014).
46. Rasmussen, S. O. et al. A stratigraphic framework for abrupt climatic changes during the last glacial period based on three synchronized Greenland ice-core records: refining and extending the INTIMATE event stratigraphy. *Quat. Sci. Rev.* **106**, 14–28 (2014).
47. Clement, A. C. & Cane, M. in *Mechanisms of Global Climate Change at Millennial Time Scales* Geophysical Monograph Series Vol. 112 (eds Clark, P. U. et al.) 363–371 (AGU, 1999).
48. Johnsen, S. J. et al. The δ^{18}O record along the Greenland Ice Core Project deep ice core and the problem of possible Eemian climatic instability. *J. Geophys. Res. Ocean* **102**, 26397–26410 (1997).
49. Steig, E. J. et al. Continuous-flow analysis of δ^{17}O, δ^{18}O, and δD of H_2O on an ice core from the South Pole. *Front. Earth Sci.* **9**, 640292 (2021).
50. McManus, J. F., Francois, R., Gherardl, J. M., Kelgwin, L. & Drown-Leger, S. Collapse and rapid resumption of Atlantic meridional circulation linked to deglacial climate changes. *Nature* **428**, 834–837 (2004).

Methods

Heinrich stadial boundaries

HSs are characterized by several criteria: (1) a weakened AMOC[5,37,50], (2) strong North Atlantic cooling[10,36], (3) EAM weakening[39,51] and (4) elevated dust (and Ca^{2+}) deposition across Greenland[13] (Extended Data Fig. 1). The HS periods we use here meet all four criteria; for practical reasons, we utilize ice-core proxies as a base for the HS boundary timing (Extended Data Table 1). Where the timing of HSs is indistinguishable from their respective DO stadial, we utilize previously published DO stadial periods[24,46] as the bounds of HS conditions. Where the distinction in timing between a DO stadial and an HS can be made, we utilize periods of elevated Greenland ice-core Ca^{2+} deposition[13]. For HS1, HS2a and HS2b, where HS conditions are meaningfully distinct, we utilize the program Rampfit[52] to identify the midpoint of changes in Ca^{2+} deposition. We utilize the abrupt warming at DO2 and the Bølling-Allerød as the termination of HS2a and HS1, respectively. For the termination of HS2b, the midpoint of Ca^{2+} reduction is used. For HS3, HS4 and HS5, where the timing of HS conditions is not distinct, we let the HS period be identical to the corresponding DO stadial period[24,46].

Measurements of GISP2 CH_4

We present measurements of atmospheric CH_4 in the GISP2 ice core on 995 unique sampling depths, performed in duplicate or triplicate. All values reported are replicate averages. Depths range from 1,740.22 m to 2,399.50 m, spanning 13,000 yr bp to 50,000 yr bp (where present is 1950) with a median age resolution of 32 yr; 915 sample depths from 1,740.22 m to 2,399.50 m were measured at Oregon State University and 80 sample depths from 2,167.89 m to 2,204.00 m were measured at Pennsylvania State University.

Measurements of CH_4 were completed using established wet-extraction techniques on roughly 60-g ice samples[23,53,54], with an average replicate difference of 2.6 ppb. Recent work has identified in situ production of CH_4 during wet-extraction measurements of dust-rich Greenland ice-core samples[23]. The contribution of in situ production scales linearly with the calcium concentration of the sample[38], at a rate of 5 ± 0.5 μmol CH_4 per mol Ca. This relationship is used to apply a correction to our record. The in situ production correction (denoted as CH_4xs) has an average of 5.5 ppb CH_4, with a maximum correction of 26.4 ppb CH_4 during the dustiest periods.

Samples were measured at Oregon State University during 4 measurement campaigns: 213 measurements were made in 2014, 439 measurements in 2016, 477 measurements in 2018, and 513 measurements in 2019. Same-depth and nearest-neighbour measurements were used to identify offsets between campaigns. No offsets were identifiable between the 2018 and 2019 campaigns, and both years were combined as the baseline for comparison against other years. A +10-ppb CH_4 offset was added to the 2014 campaign, and a +5-ppb offset for the 2016 campaign. The CH_4 standard tank used for calibrating measurements was changed between the 2016 and 2018 sample campaigns, providing a potential origin for these offsets. The four nearest-neighbour samples were measured for interlaboratory calibration between Oregon State University and Pennsylvania State University and did not suggest any offsets between labs.

Measurements of GISP2 $\delta^{15}N–N_2$

We present measurements of $\delta^{15}N–N_2$ ($\delta^{15}N$) in the GISP2 ice core from 643 unique sampling depths, with 312 measurements completed in replicate. Where available, reported values are replicate averages. Measurements were conducted at the Ice Core Noble Gas Laboratory of the Scripps Institution of Oceanography on approximately 12-g samples using established wet-extraction techniques[55–57]. Measurements are calibrated to contemporary La Jolla air. Samples span 12,500 yr bp to 50,000 yr bp, with a median age resolution of 38 yr. Sample resolution is increased during HSs, with a median resolution of 18 yr. These measurements compliment previous GISP2 $\delta^{15}N$ measurements over the Holocene and select DO events[22,26,58–60], providing a complete record of GISP2 $\delta^{15}N$ over the past 50,000 yr bp.

Stated uncertainty for samples measured before 2009 range between 0.003‰ and 0.004‰, whereas the samples presented here have a pooled replicate standard deviation of 0.0025‰. The complete GISP2 $\delta^{15}N$ dataset results in 1,665 unique samples depths, with a weighted-average precision of 0.0031‰.

Samples were measured at the Scripps Institution of Oceanography for $\delta^{15}N$ over three campaigns: 193 samples were measured in 2017, 42 samples measured in 2018, and 418 were measured in 2020. Same-depth and nearest-neighbour samples were measured to identify potential offsets between the 2017/2018 and 2020 measurements. No offsets were identified for the 2017 sample campaign, and a +0.006‰ offset was added to the 2018 sample measurements.

Comparison of the 2017–2020 dataset with previously published data measured before 2010 using nearest-neighbour or same-depth samples also identified systematic offsets possibly due to gas loss during storage. Overlapping data in the intervals of 1,824–1,903 m, 2,220–2,244 m and 2,355–2,366 m was used for calibration between this study and previously published datasets. These intervals cover HS1, DO8 and DO12 respectively. Through this comparison, a +0.01‰ offset was applied to the 2017–2020 sample campaigns. This difference could be the result of gas loss during sample storage. In addition, it could be due to subtle calibration differences as samples are normalized against La Jolla air contemporaneous with each sample campaign.

Gas- and ice-phase synchronization

Abrupt changes in atmospheric CH_4 can be utilized to synchronize the gas-age chronologies of ice cores[24,54,61–64]. We identify shared millennial to multi-decadal variations in CH_4 between the WD and GISP2 records. The WD ice core serves as the ideal Antarctic target core, as there exists a centimetre-scale CH_4 record that removes the potential impact of signal aliasing[17]. In addition, the core has a stable and well resolved Δage—enhancing certainty in chronological synchronization. Through this stratigraphic matching of well mixed gas-phase proxies, the transference of the WD2014 gas-age timescale to GISP2 during stadial and interstadial conditions is possible[24,25]. Over the 50,000 yr of overlapping WD and GISP2 CH_4 data coverage, we identify 151 gas-phase matchpoints in CH_4. Extended Data Fig. 8 highlights an example of coherent centennial-scale variability alongside abrupt-event synchronization during the DO12 interstadial.

Abrupt-event features include DO stadial-to-interstadial transitions and HEs. These matches were constructed by calculating pre- and post-event averages in both cores, then assigning the midpoint between averages as a synchronous match. Centennial-scale features represent 10–30-ppb background variations in CH_4 that are well resolved in both the WD and GISP2 records. These matches were first identified by visual inspection, often as the midpoint or trough of centennial features. Centennial variations used for synchronization are observed primarily during interstadial periods. In the Greenland CH_4 record, stadial periods have a higher contribution of CH_4xs[23] and increased smoothing owing to low accumulation that complicates synchronization.

Centennial- and millennial-scale matches are then verified using an automated correlation scheme that samples 1,000 iterations of random perturbations within a 50-yr window around each matchpoint. The perturbed chronology is then applied to the GISP2 CH_4 record. Both the GISP2 and WD CH_4 records are then highpass-filtered at a 100-yr cut-off frequency and correlated. The perturbation that maximizes the correlation is recorded as the optimal match. The average optimized perturbation from the visual matchpoint is ±14 yr, indicating robust gas-phase matches.

Uncertainty for gas-based matches is a combination of four factors: the sample resolution of the GISP2 and WD CH_4 records at the age of the matchpoint, the uncertainty in WD Δage, the ability to visually identify matches and the climate conditions associated with the match. For WD, we set the sample resolution value to 5 yr; for GISP2 it is 41 yr on average. The ability to determine a visual match was evaluated through an automated correlation scheme, and the average distance to the optimal match was 14 yr. The climate period uncertainty is a prescribed estimate of uncertainty due to changes in local processes, such as a firn smoothing or the CH_4xs contribution. During cold and dusty stadial conditions, high values of Δage and an elevated contribution of CH_4xs lead to greater uncertainty in the observed structure of CH_4. We assign this component a maximum uncertainty of 50 yr during the Last Glacial Maximum, and values between 25 yr and 40 yr for other stadials. The climate period contribution is at a minimum value during interstadials and abrupt transitions, where there is limited smoothing due to firn processes and small contributions of CH_4xs. A value of 25 yr is set for interstadial conditions, and 10 yr for abrupt transitions. We define the total temporal uncertainty for each gas-phase matchpoint as the root-mean-square sum of the four components.

Geochemical proxies of volcanic activity have been previously used to synchronize ice-age chronologies across Greenland[26] or Antarctica[9,65–68]. Recent work has identified interhemispheric volcanic signals, allowing for ice-phase synchronizations between Greenland and Antarctica[27,67]. We utilize direct ties between GISP2 and WD, and additionally transfer ties between NGRIP and EDML to GISP2 and WD, respectively. Through this direct and correlated ice-phase volcanic synchronization, 106 ice-age stratigraphic matches between GISP2 and WD can be identified. Of these, 81 are during the last glacial period, covering the period of 12 kyr bp to 59 kyr bp. We define the uncertainty of these volcanic matches as the difference in uncertainty of the layer-counted Greenland Ice Core Chronology 2005 (GICC05) chronology between nearest volcanic matches, as the matches rely on the proximity to nearby matches rather than the absolute age of the match.

With both gas- and ice-phase synchronizations, GISP2 Δage can be empirically calculated. We define the uncertainty in the empirical Δage constraints as the root-mean-square sum of the gas-phase uncertainty components (sample resolution, WD Δage, visual match uncertainty and climate conditions) and the ice-phase components.

Chronology development

At present, the best available GISP2 chronology is the Greenland ice-core chronology 2005, or GICC05[69–71]; the best WD chronology is the WD2014 chronology[24,25]. GICC05 and WD2014 use annual layer counting for the past 60 kyr and 31 kyr, respectively. Using the available bipolar volcanic matchpoints, we construct a bipolar ice chronology (BIC) that synchronizes the GISP2 and WD chronologies. The BIC uses the WD2014 layer count for the past 31 kyr and the GICC05 layer count for 31–60 kyr bp—these two chronologies are in agreement at 31 kyr, making the transition a natural one. We use a cubic smoothing spline (implemented via the MATLAB csaps function) to transfer the existing chronologies onto the BIC.

There is a gap in bipolar volcanic matchpoints between 16.4 ky bp and 24.6 kyr bp, an interval that includes the HS1 onset. The available GISP2 GICC05 timescale[26] places the HS1 onset as seen in GISP2 calcium, $\delta^{15}N$ and CH_4 at around 17.5 kyr bp; this event is typically dated to about 17.8 kyr in other archives. This suggests a strong undercount of the annual layering through the early HS1 in GICC05; this may be explained by recent modelling work that suggests a loss of winter precipitation during HS1[20] that would severely hamper the ability to detect annual layers. In the absence of bipolar volcanic matchpoints at the HS1 onset, we instead rely on bipolar CH_4 matching. We have a good constraint on the GISP2 Δage at the HS1 onset as it is found that both the gas ($\delta^{15}N$) and ice (Ca) phases are synchronous with a bipolar CH_4 matchpoint at that time (onset of deglacial CH_4 increase). The need to use bipolar CH_4 rather than volcanic matching results in larger synchronization uncertainty in this interval, and hence a larger uncertainty in the empirical GISP Δage. The difference between the BIC and the original ice-core timescales is shown in Extended Data Fig. 3.

Firn model climate reconstructions

To reconstruct Greenland temperature and accumulation, we adopt an inverse dynamical firn densification strategy[24,29,30,72]. Through this, temperature and accumulation histories are optimized to best match the observations of $\delta^{15}N$ and Δage through an automated algorithm. Previous studies utilizing these techniques have been limited by $\delta^{15}N$ and Δage data availability outside of abrupt millennial-scale features. In particular, empirical Δage estimates were needed to provide climate reconstructions independent of $\delta^{18}O_{ice}$ variability. Critically, we make two advances in this study: (1) high-resolution measurements of $\delta^{15}N$ over the past 50,000 yr greatly increases data availability both during and in between DO transitions; (2) empirical Δage constraints are available throughout the past 50,000 yr via interhemispheric gas- and ice-phase synchronization.

A detailed description of the firn model is provided in ref. 72. Briefly, we utilize a coupled firn densification and heat diffusion model to simulate the response of the firn layer to site surface temperature and accumulation. Densification physics is based on a dynamical description of the Herron–Langway model[73]; updated firn thermal properties[74]; and the lock-in density is set at 14 kg m^{-3} below the close-off density[75,76]. In the forwards model scenario, site temperature (T_{site}) and accumulation (A) are used to generate an output of $\delta^{15}N$ and Δage. An initial guess for T_{site} and A is based on linear scaling of a Summit climate template. This template is based on the average of $\delta^{18}O$ and Ca^{2+} concentrations scaled to an equivalent change in $\delta^{18}O$. First, Ca^{2+} concentrations are transformed via $-1\log(Ca^{2+})$ as this produces similarly structured variability to the smoothed $\delta^{18}O$ record Next, we calculate the linear regression of $-1\log(Ca^{2+})$ to $\delta^{18}O$ for Summit. This allows us to transform $-1\log(Ca^{2+})$ into units of $\delta^{18}O$, making it possible to average them together. Through this method, we can average four similarly varying records (GISP2 and GRIP $\delta^{18}O$ and transformed Ca^{2+}) and strongly improve the signal-to-noise ratio for our initial template.

Here we utilize the model in an inverse mode, where the forwards model is run repeatedly to find the T_{site} and A histories that optimize the fit of simulated $\delta^{15}N$ and Δage histories with data. Starting from linearly scaled versions of the Summit climate template, the T_{site} and A forcings are modified in a gradient method to identify the optimal solution[24,26,29,72], seeking to minimize the root-mean-square cost function:

$$\mathrm{RMSD} = \sqrt{\frac{1}{N}\sum_{n=1}^{N}\frac{(m_n - d_n)^2}{\sigma_n^2}} \tag{1}$$

where N is the total number of data points, d_n is the measured data point at depth n ($\delta^{15}N$ and Δage), m_n is the output at modelled depth n, and σ_n is the precision of d_n. For $\delta^{15}N$, σ_n reflects the pooled standard deviation of replicate measurements; for Δage, σ_n reflects the uncertainty in the gas-phase matchpoint used to reconstruct that Δage constraint.

Point-to-point variability in the $\delta^{15}N$ data frequently exceeds this analytical uncertainty owing to physical processes that are not fully represented in the firn model, such as firn layering, stochastic variations in the depth of bubble trapping or variability in the depth of the convective-zone thickness[77]. Roughly 10-cm samples were selected for $\delta^{15}N$ measurements to reduce the impact of these subcentimetre-scale signals[78]. Limited degrees of freedom in adjusting the temperature and accumulation histories prevents the model from overfitting this noise present in $\delta^{15}N$ records. Partly owing to trapping noise, the model is unable to fit all the $\delta^{15}N$ data within the stated analytical precision. Increasing the precision σ_n in equation (1) to account for these physical noise processes will lower the numerical value of the final RMSD obtained, but not meaningfully change the climate reconstructions themselves.

Heinrich event response experiments

To investigate the Greenland climate response to an idealized HE, we utilize a series of experiments centred on HE1. As there is no abrupt climatic feature in $\delta^{15}N$ coincident with the HE1 abrupt CH_4 increase, the aim of these experiments is to identify an upper limit on cooling that is allowed by the $\delta^{15}N$ and Δage constraints. The timing of the 16.2-kyr CH_4 feature that we attribute to HE1 coincides with the HE1 detrital layer in North Atlantic sediments[11].

For our experiments, we define two families of forcings that we refer to as 'peak' and 'sustained'. A peak forcing is triangular in shape, and can vary based on onset duration, recovery duration and peak magnitude. A sustained forcing is trapezoidal in shape, and can vary through peak magnitudes, duration of peak magnitudes, and rapid onsets and recoveries of symmetric duration. Peak magnitudes for both experiment families range from 0 °C to −3 °C, in 0.25 °C steps. All experiment forcings are shown Extended Data Fig. 4. The forcing onset is synchronous with the onset of the CH_4 feature in the WD record during HS1, at 16,130 ± 150 yr bp.

These HE anomaly forcings are then applied to the initial temperature history of the firn model.

This experimental temperature history is utilized as a template for the iterative forwards model scenario, such that the model will attempt to optimize new modelled output with data observations. Experiments are evaluated based on the RMSD (equation (1)) between observed data and model output over a window of 390 yr, or the period of unique $\delta^{15}N$ variability surrounding the HS1 CH_4 feature. Each experiment is then compared against the RMSD for the 0 °C control forcing run and evaluated for improvements to fit over the same window.

The results show that the optimal family of forcing is a slow onset with a fast recovery and indicates only events with a magnitude of 1.0 °C or less improve the model response with respect to the control (Extended Data Fig. 4). Events of a greater magnitude quickly diverge from the observed data during both the event and the event recovery. This upper bound on the HE temperature response is well within the natural background variability of Greenland climate[31,79], and therefore we do not consider it climatically meaningful.

We emphasize that the results shown here provide only a probable upper limit to the magnitude of the Greenland climate response, with little insight into other archives that are impacted by these events. However, these experiments can provide qualitative insight into the characteristics of the Greenland climatic response to HEs, such as the upper bound on magnitude and duration.

Stacking methods

We construct composite (or stacked) records for the DO and HE events. In these stacked records, we align the individual events, and then average them to identify their common climatic signal. The stacking method used here is the same as in previous studies[9,27,80], with details in the original references. In the stacking, we use DO events 0 (Holocene onset) to 13, aligning the events at the midpoint of the Greenland ice-core Ca transition. We use HE1 to HE5, aligning the events at the midpoint of the abrupt CH_4 increases.

The Antarctic lag during DO variability shown here (122 ± 24 yr) is smaller than previous estimates using bipolar CH_4 synchronization (218 ± 92 yr)[80], because the original work underestimates WD Δage by about 50 yr, and assumes a 56-yr delay of CH_4 behind $\delta^{18}O$; our work suggests a 29-yr delay instead (Extended Data Fig. 9).

The spatial magnitude of $\delta^{18}O$ change across Antarctica was identified as the difference of pre- and post-event averages in the stack for each site. The pre-event average is over the interval of −300 yr to −50 yr. The post-event average is over the interval from 200 yr to 450 yr. The per-site stacks are computed using the same method as the Antarctic-wide stack.

To identify a meaningful change in slope of the Antarctic average $\delta^{18}O$ stack, we utilize the program Breakfit[81]. Although this method is valuable for identifying statistically significant changes in the trends of data, it is susceptible to significant variability based on user selections. The change in trend of the Antarctic average $\delta^{18}O$ stack is dependent on the selection of an initial bound. If the Breakfit algorithm begins at −1,200 yr before the CH_4 midpoint, the inflection occurs at −101 yr. If it begins at −600 yr before the CH_4 midpoint, the inflection occurs at −43 yr. Here we take the average value of these two extremes and set the inflection at −72 yr. The uncertainty of Δage covers the window of these two extremes at ±76 yr. As such, we propose that the average, when combined with the uncertainty, meaningfully covers the range of possible inflections.

Data availability

GISP2 $\delta^{15}N-N_2$ and CH_4 data are available via the NSF Arctic Data Center (https://doi.org/10.18739/A2639K65M) and in the Supplementary Data. Source data are provided with this paper.

Code availability

The code for stacking the records is available with ref. 80.

51. Wang, Y. J. et al. A high-resolution absolute-dated late Pleistocene monsoon record from Hulu Cave, China. *Science* **294**, 2345–2348 (2001).
52. Mudelsee, M. Ramp function regression: a tool for quantifying climate transitions. *Comput. Geosci.* **26**, 293–307 (2000).
53. Mitchell, L. E., Brook, E. J., Sowers, T., McConnell, J. R. & Taylor, K. Multidecadal variability of atmospheric methane, 1000–1800 C.E. *J. Geophys. Res. Biogeosci.* **116**, G02007 (2011).
54. Mitchell, L., Brook, E., Lee, J. E., Buizert, C. & Sowers, T. Constraints on the late Holocene anthropogenic contribution to the atmospheric methane budget. *Science* **342**, 964–966 (2013).
55. Sowers, T., Bender, M. & Raynaud, D. Elemental and isotopic composition of occluded O_2 and N_2 in polar ice. *J. Geophys. Res.* **94**, 5137–5150 (1989).
56. Petrenko, V. V., Severinghaus, J. P., Brook, E. J., Reeh, N. & Schaefer, H. Gas records from the West Greenland ice margin covering the Last Glacial Termination: a horizontal ice core. *Quat. Sci. Rev.* **25**, 865–875 (2006).
57. Severinghaus, J., Beaudette, R., Headly, M., Taylor, K. & Brook, E. Oxygen-18 of O_2 records the impact of abrupt climate change on the terrestrial biosphere. *Science* **324**, 1431–1435 (2009).
58. Severinghaus, J. P. & Brook, E. J. Abrupt climate change at the end of the last glacial period inferred from trapped air in polar ice. *Science* **286**, 930–934 (1999).
59. Grachev, A. M., Brook, E. J. & Severinghaus, J. P. Abrupt changes in atmospheric methane at the MIS 5b–5a transition. *Geophys. Res. Lett.* **34**, L20703 (2007).
60. Kobashi, T., Severinghaus, J. P. & Kawamura, K. Argon and nitrogen isotopes of trapped air in the GISP2 ice core during the Holocene epoch (0–11,500 B.P.): methodology and implications for gas loss processes. *Geochim. Cosmochim. Acta* **72**, 4675–4686 (2008).
61. Blunier, T. & Brook, E. J. Timing of millennial-scale climate change in Antarctica and Greenland during the last glacial period. *Science* **291**, 109–112 (2001).
62. EPICA Community Members One-to-one coupling of glacial climate variability in Greenland and Antarctica. *Nature* **444**, 195–198 (2006).
63. Epifanio, J. A. et al. The SP19 chronology for the South Pole ice core—Part 2: gas chronology, Δage, and smoothing of atmospheric records. *Clim. Past* **16**, 2431–2444 (2020).
64. Bender, M. et al. Climate correlations between Greenland and Antarctica during the past 100,000 years. *Nature* **372**, 663–666 (1994).
65. Severi, M. et al. Synchronisation of the EDML and EDC ice cores for the last 52 kyr by volcanic signature matching. *Clim. Past* **3**, 367–374 (2007).
66. Severi, M., Udisti, R., Becagli, S., Stenni, B. & Traversi, R. Volcanic synchronisation of the EPICA-DC and TALDICE ice cores for the last 42 kyr bp. *Clim. Past* **8**, 509–517 (2012).
67. Veres, D. et al. The Antarctic Ice Core Chronology (AICC2012): an optimized multi-parameter and multi-site dating approach for the last 120 thousand years. *Clim. Past* **9**, 1733–1748 (2013).
68. Bazin, L. et al. An optimized multi-proxy, multi-site Antarctic ice and gas orbital chronology (AICC2012): 120–800 ka. *Clim. Past* **9**, 1715–1731 (2013).
69. Rasmussen, S. O. et al. A new Greenland ice core chronology for the last glacial termination. *J. Geophys. Res. Atmos.* **111**, D06102 (2006).
70. Andersen, K. K. et al. The Greenland Ice Core Chronology 2005, 15–42 ka. Part 1: constructing the time scale. *Quat. Sci. Rev.* **25**, 3246–3257 (2006).
71. Svensson, A. et al. The Greenland Ice Core Chronology 2005, 15–42 ka. Part 2: comparison to other records. *Quat. Sci. Rev.* **25**, 3258–3267 (2006).
72. Buizert, C. et al. Greenland temperature response to climate forcing during the last deglaciation. *Science* **345**, 1177–1180 (2014).
73. Herron, B. M. M. & Langway, C. C. Firn densification: an empirical model. *J. Glaciol.* **25**, 373–385 (1980).
74. Calonne, N. et al. Thermal conductivity of snow, firn, and porous ice from 3-D image-based computations. *Geophys. Res. Lett.* **46**, 13079–13089 (2019).
75. Martinerie, P. et al. Air content paleo record in the Vostok ice core (Antarctica): a mixed record of climatic and glaciological parameters. *J. Geophys. Res.* **99**, 10565–10576 (1994).

76. Blunier, T. & Schwander, J. Gas enclosure in ice: age difference and fractionation. In *Physics of Ice Core Records*, edited by: Hondoh, T., Hokkaido University Press, Sapporo, 307–326 (2000).
77. Rosen, J. L. et al. An ice core record of near-synchronous global climate changes at the Bølling transition. *Nat. Geosci.* **7**, 459–463 (2014).
78. Orsi, A. J. *Temperature Reconstruction at the West Antarctic Ice Sheet Divide, for the Last Millennium, from the Combination of Borehole Temperature and Inert Gas Isotope Measurements*. DPhil dissertation, Univ. California, San Diego (2013); https://escholarship.org/uc/item/02g3c5fq.
79. Kobashi, T. et al. Persistent multi-decadal Greenland temperature fluctuation through the last millennium. *Climatic Change* **100**, 733–756 (2010).
80. Buizert, C. et al. Precise interpolar phasing of abrupt climate change during the last ice age. *Nature* **520**, 661–665 (2015).
81. Mudelsee, M. Break function regression: a tool for quantifying trend changes in climate time series. *Eur. Phys. J. Spec. Top.* **174**, 49–63 (2009).
82. Lisiecki, L. E. & Stern, J. V. Regional and global benthic $\delta^{18}O$ stacks for the last glacial cycle. *Paleoceanography* **31**, 1368–1394 (2016).
83. Dahl-Jensen, D. et al. Eemian interglacial reconstructed from a Greenland folded ice core. *Nature* **493**, 489–494 (2013).
84. Erhardt, T. et al. Decadal-scale progression of the onset of Dansgaard–Oeschger warming events. *Clim. Past* **15**, 811–825 (2019).
85. Cuffey, K. M. & Clow, G. D. Temperature, accumulation, and ice sheet elevation in central Greenland through the last deglacial transition. *J. Geophys. Res. Ocean.* **102**, 26383–26396 (1997).
86. Buizert, C. et al. Greenland-wide seasonal temperatures during the last deglaciation. *Geophys. Res. Lett.* **45**, 1905–1914 (2018).
87. Liu, Z. et al. Transient simulation of last deglaciation with a new mechanism for Bølling–Allerød warming. *Science* **325**, 310–314 (2009).
88. Obase, T. & Abe-Ouchi, A. Abrupt Bølling–Allerød warming simulated under gradual forcing of the last deglaciation. *Geophys. Res. Lett.* **46**, 11397–11405 (2019).

Acknowledgements The work was supported financially by the US National Science Foundation grant 1702920 to C.B. and E.J.B.; NSF grant 2102944 to C.B.; the Global Climate Change Foundation (GCCF24, to C.B.) and the Gary Comer Science and Education Foundation (CP116, to J.P.S.). We thank the NSF ice-core facility (ICF) for their curation and assistance in preparation of ice-core samples.

Author contributions The paper was prepared by K.C.M. and C.B. The data analysis was conducted by K.C.M., C.B., J.S.E. and E.J.B. The chronology was developed by C.B. and K.C.M. The methane data were produced by K.C.M., C.B., E.J.B., J.S.E., B.R.-Y., M.L.K. and T.A.S. The $\delta^{15}N$ data were produced by R.B. and J.P.S. All authors contributed to the final paper.

Competing interests The authors declare no competing interests.

Additional information
Supplementary information The online version contains supplementary material available at https://doi.org/10.1038/s41586-023-05875-2.
Correspondence and requests for materials should be addressed to Kaden C. Martin.
Peer review information *Nature* thanks the anonymous reviewers for their contribution to the peer review of this work. Peer reviewer reports are available.
Reprints and permissions information is available at http://www.nature.com/reprints.

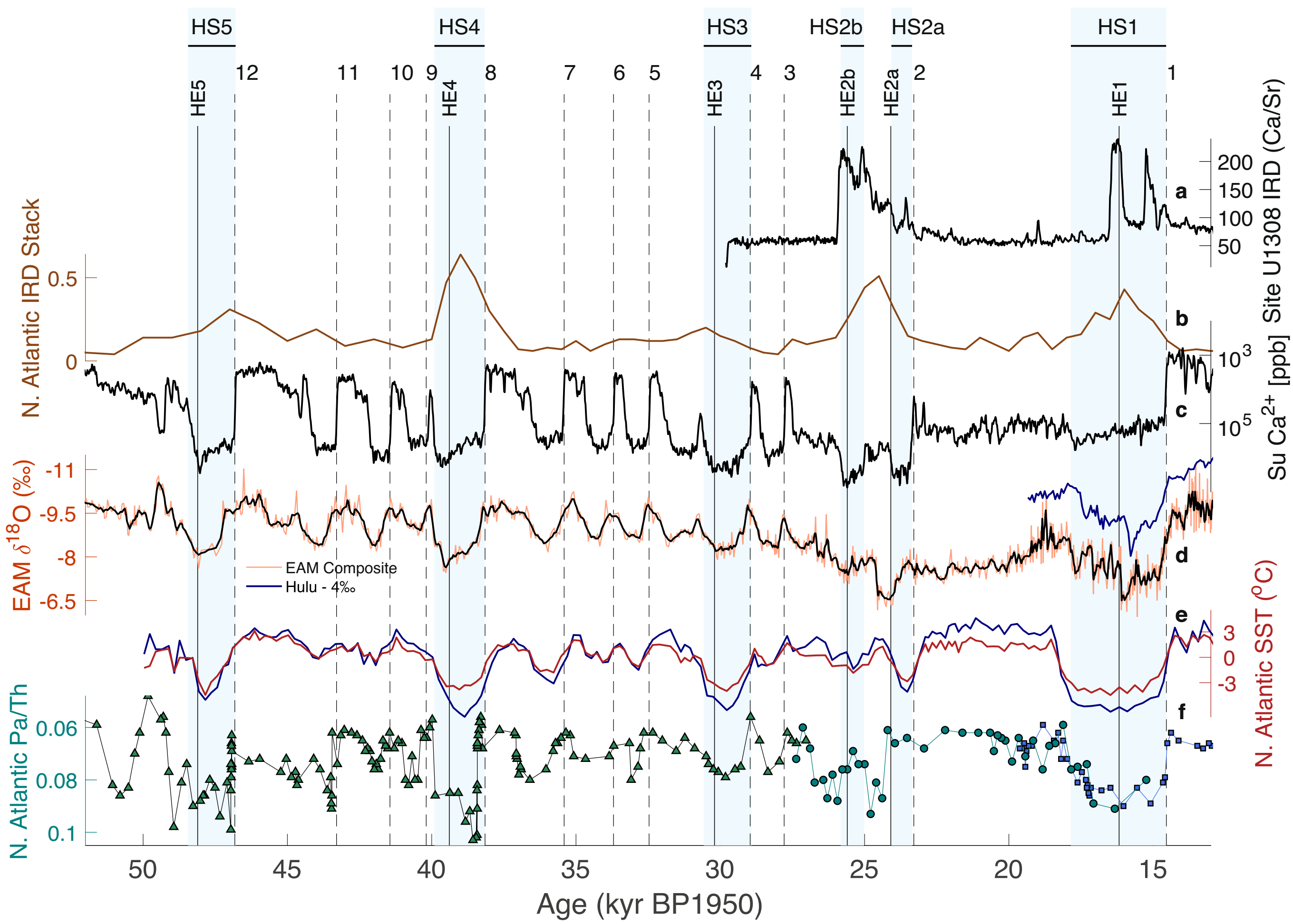

Extended Data Fig. 1 | Far- and near-field climate proxies indicative of Heinrich Stadial conditions. **a**, U1308 IRD (black; ref. 11). **b**, North Atlantic IRD Stack with arbitrary units (brown; ref. 82). **c**, Summit Calcium (note concentration units on reversed axis with log scale, black; ref. 38). **d**, Speleothem composite of East Asian Monsoon strength (orange is raw data, black is 5-point running average; ref. 39) and Hulu $\delta^{18}O$ (blue, from stalagmite PD offset by −4‰; ref. 51). **e**, North Atlantic stack (dark red) and Iberian Margin (dark blue) SST reconstruction transferred from GICC05 to BIC (ref. 36). **f**, Bermuda Rise $^{231}Pa/^{230}Th$ (blue squares[50], teal circles[37], green triangles[5]). Light blue bars denote the duration of Heinrich Stadials. Solid and dashed vertical lines indicate timing of Heinrich Events and DO stadial to interstadial transitions, respectively, inferred by the midpoint of CH_4 features.

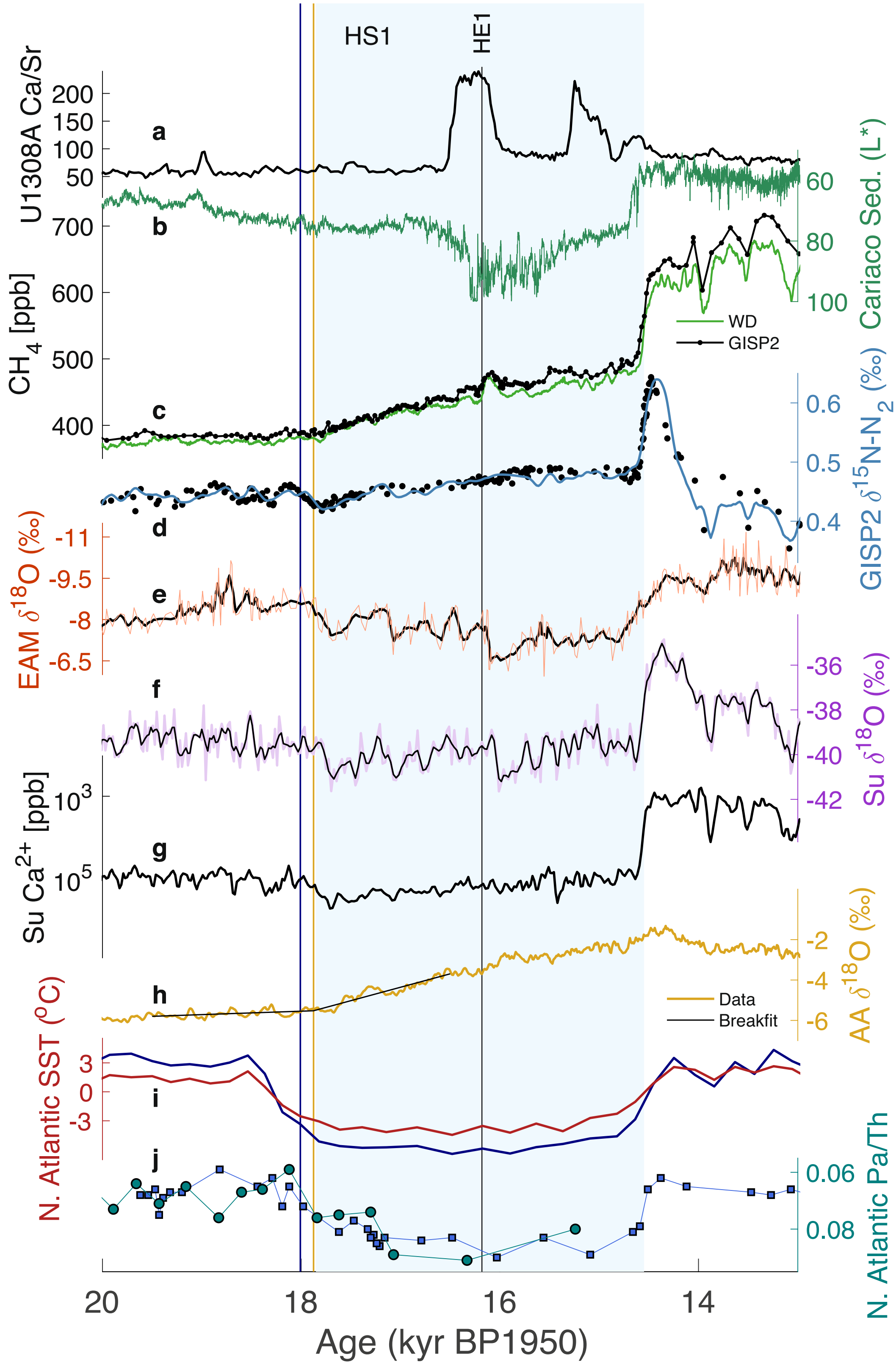

Extended Data Fig. 2 | Paleoclimate records during HS1. a, North Atlantic IRD from site U1308A (black; ref. 11). **b**, Cariaco Basin Sediment Reflectance (note reversed axis; teal; ref. 19). **c**, WD CH_4 (green; ref. 17) and GISP2 CH_4 (black; this study). **d**, GISP2 $\delta^{15}N$ (modeled reconstruction in blue, data in black; this study). **e**, Speleothem composite of East Asian Monsoon strength (orange is raw data, black is 5-point running average; ref. 39). **f**, Summit $\delta^{18}O$ (GISP2 and GRIP average, purple; ref. 48). **g**, Summit Ca^{2+} (black; ref. 38). **h**, 6-core Antarctic average $\delta^{18}O$ (gold; refs. 9,49). **i**, North Atlantic stack (dark red) and Iberian Margin (dark blue) SST reconstruction transferred from GICC05 to BIC (ref. 36). **j**, Bermuda Rise $^{231}Pa/^{230}Th$ (blue squares[50], teal circles[37]); The light blue bar denotes duration of Heinrich Stadial 1. Solid black line indicates timing of Heinrich Event 1 based on IRD and CH_4. The vertical dark blue line is the midpoint of Greenland $\delta^{15}N$ change at 18008 years BP, which is synchronous with the midpoint of cooling. The vertical gold line indicates the inflection of 6-core Antarctic $\delta^{18}O$ stack identified by Breakfit[81] at 17875 years BP.

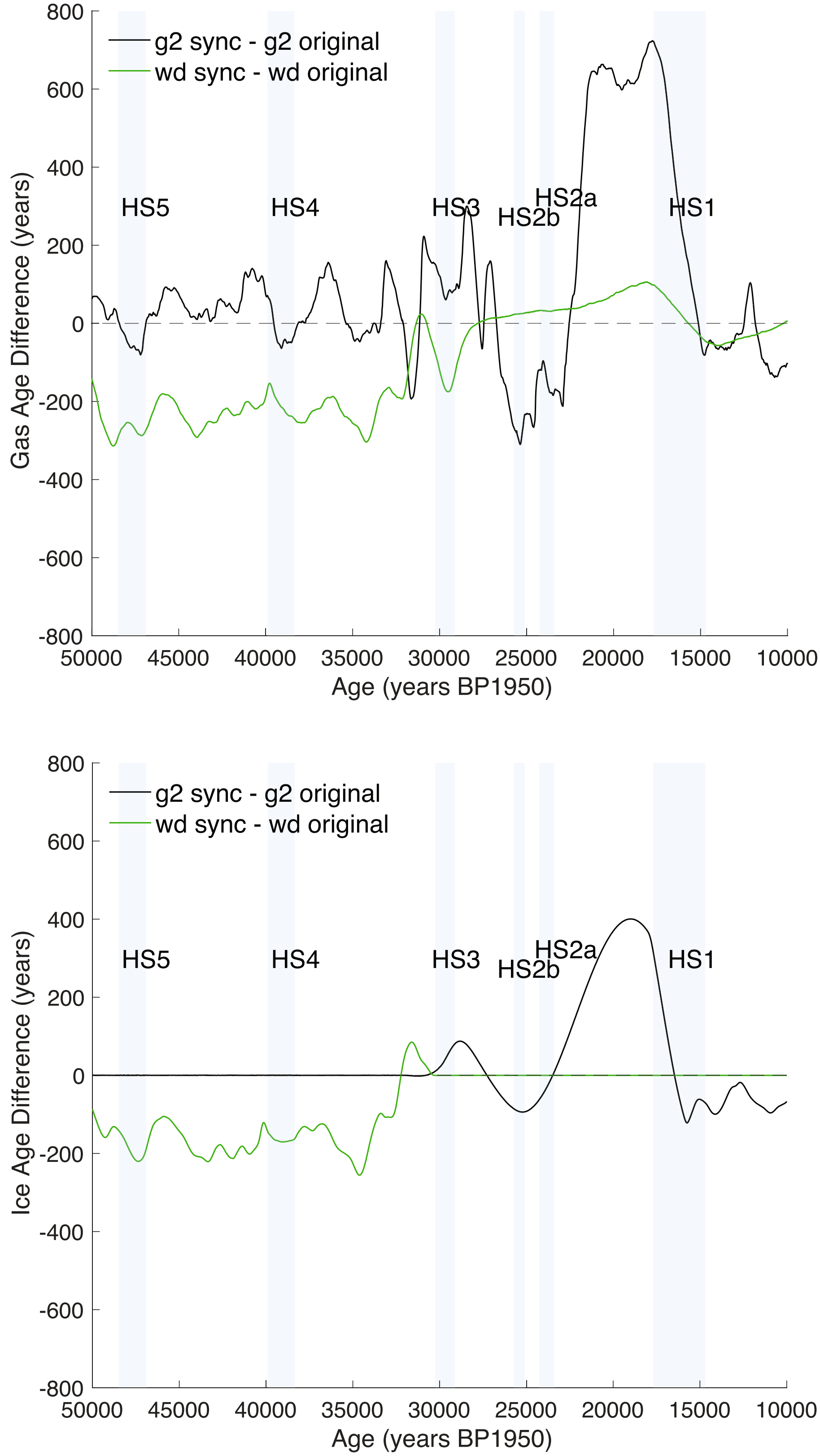

Extended Data Fig. 3 | Offsets between the synchronized and original chronologies for WD and GISP2. Upper panel: Gas age differences between synchronized chronology and GICC05 (black) and WD2014 (green). Changes after 31ka in gas age differences are largely due to removing the 1.0063 scaling factor in WD[24]. Lower panel: Ice age differences between synchronized chronology and GICC05 (black) and WD2014 (green). Note that there is a 0-year ice age difference in GISP2 older than 31,000 years; WD has a 0-year ice age offset from 0-31,000 years.

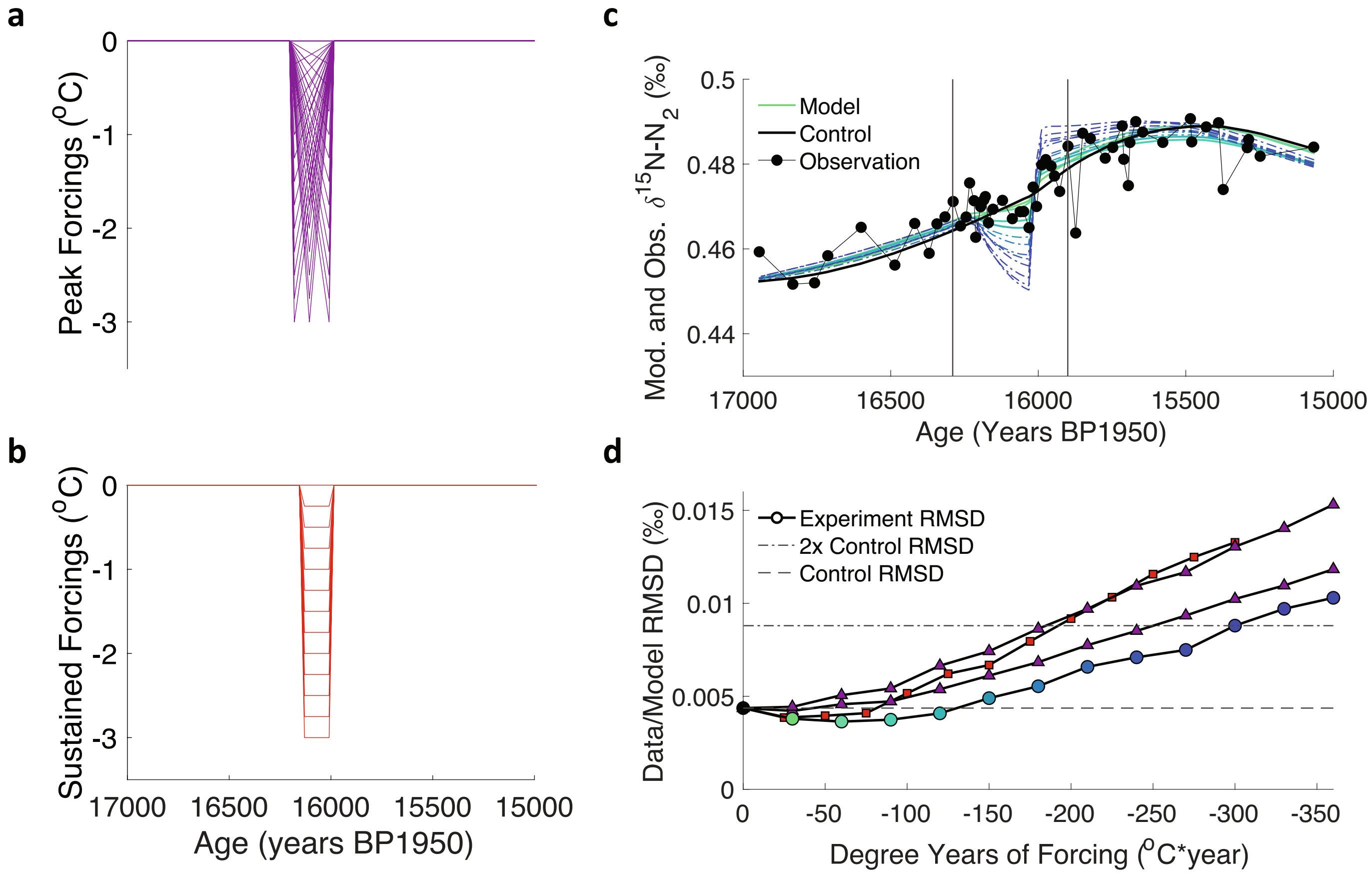

Extended Data Fig. 4 | Heinrich Event Sensitivity experiment results and experiment forcings. a, magnitude and duration of forcings for peaked/triangular experiments**. b**, magnitude and duration of forcings for sustained/square experiments. **c**, $\delta^{15}N$ data (black circles), control experiment (black line), and experimental output for a range of peaked forcings with abrupt recovery (colored lines). Cooler colors indicate more extreme temperature anomalies, dashed curves indicate model output outside of the control RMSD**. d**, Data to model RMSD evaluation for a range of model runs. Each circle corresponds to the integrated temperature forcing for an experiment, green to blue color gradient corresponds to panel C, cool and warm colors correspond to example runs from peak and sustained forcings respectively.

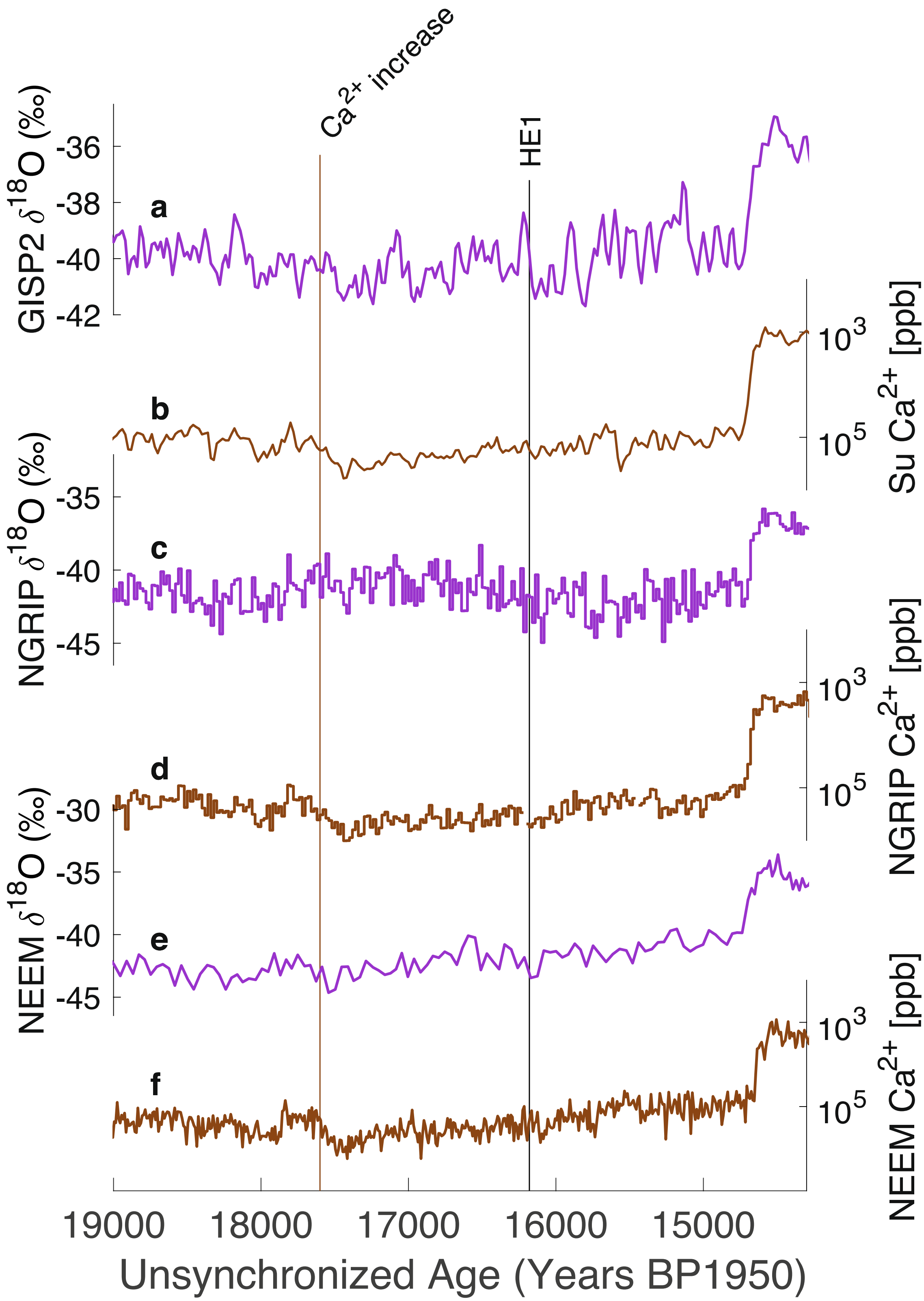

Extended Data Fig. 5 | Comparison between Greenland ice core records over Heinrich Stadial 1. a, GISP2 $\delta^{18}O$ (purple; ref. 26). **b**, GISP2 Ca^{2+} (brown; ref. 26). **c**, NGRIP $\delta^{18}O$ (purple; ref. 26). **d**, NGRIP Ca^{2+} (brown; ref. 26). **e**, NEEM $\delta^{18}O$ (purple; ref. 83). **f**, NEEM Ca^{2+} (brown; ref. 84). Note that Ca^{2+} is in concentration units on a reverse log scale, on their original chronologies[26]. Vertical brown line indicates a cohesive change in Ca^{2+} across all cores at the midpoint of abrupt Ca^{2+} increase. Vertical solid line indicates timing of HE1 inferred from CH_4.

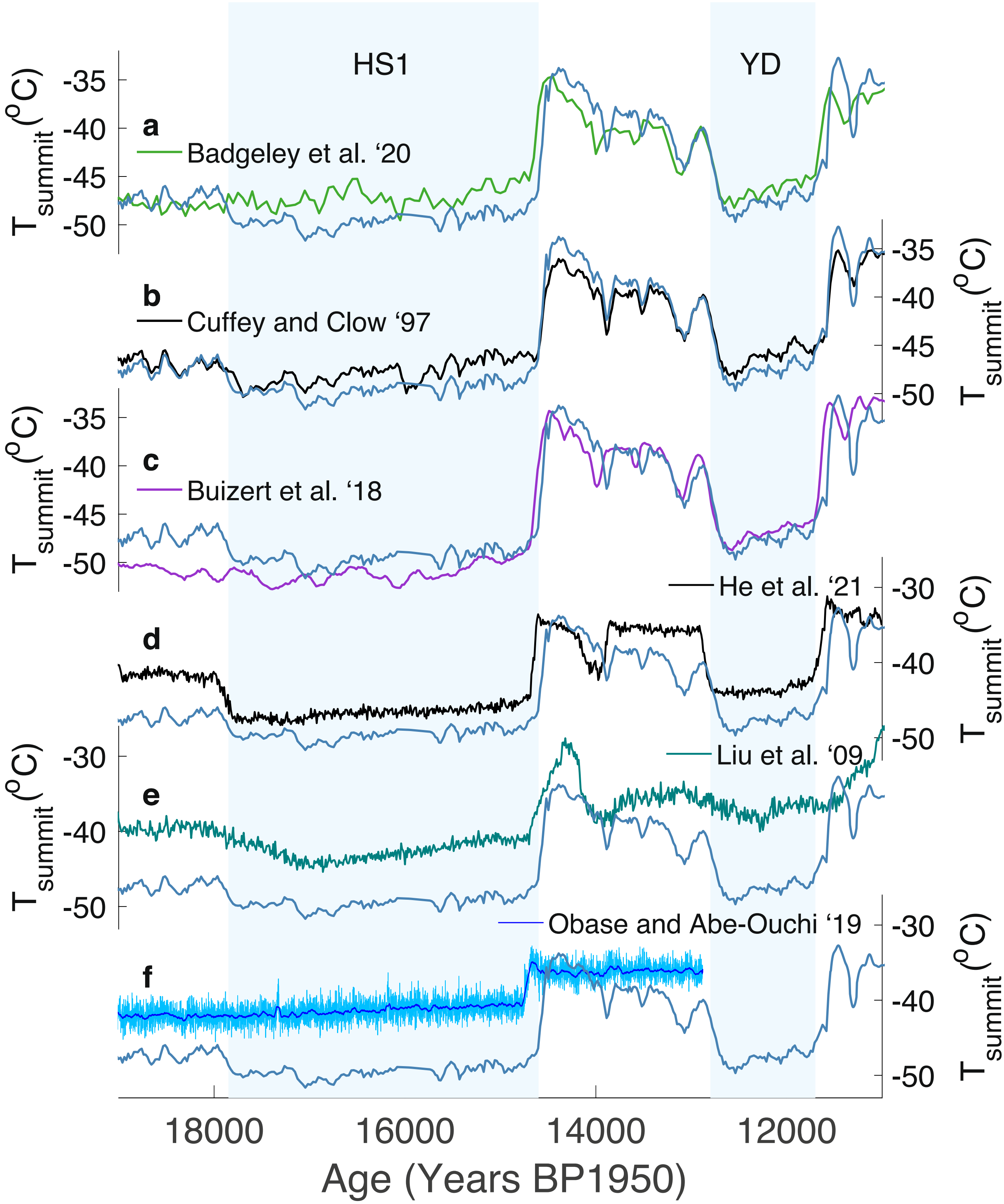

Extended Data Fig. 6 | Comparison between geochemical and climate model temperature reconstructions at Summit, Greenland. The firn model reconstruction produced in this study (blue) is compared against existing reconstructions. **a**, Badgeley et al. (2020) reconstruction using data assimilation with δ^{18}Oice (green; ref. 34). **b**, Cuffey and Clow (1997) δ^{18}O-T scaling applied to our Summit δ^{18}O and scaled Ca^{+2} stack (black; ref. 85). **c**, Buizert et al. (2018) firn reconstruction (purple; ref. 86). **d**, He et al. (2021) reconstruction accounting for modified seasonality of precipitation (black; ref. 20). **e**–**f**, transient, globally coupled climate model simulations of Liu et al. (2009) (teal; ref. 87) and Obase and Abe-Ouchi (2019) (light blue; ref. 88).

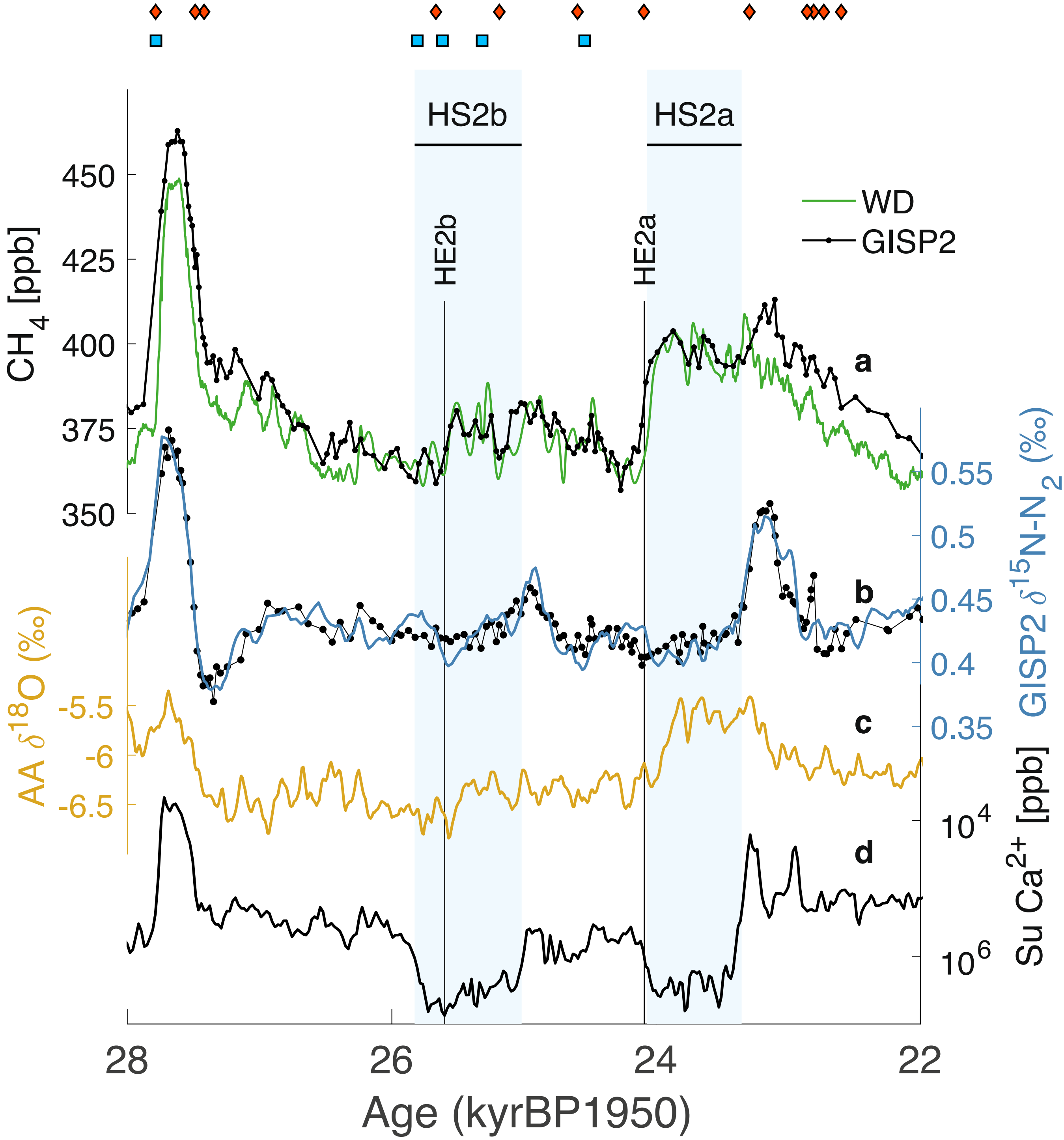

Extended Data Fig. 7 | Phasing of Antarctic $\delta^{18}O$ and CH_4 during HS2b and HS2a. **a**, WD CH_4 (green; ref. 17) and GISP2 CH_4 (black; this study). **b**, GISP2 $\delta^{15}N$ (modeled reconstruction in blue, data in black; this study). **c**, Antarctic average $\delta^{18}O$ (gold; ref. 9). **d**, Summit Ca^{2+} (black; ref. 38). Light blue bars denote Heinrich Stadials, and dashed vertical lines indicate Heinrich Event timings inferred by CH_4 peaks for HE2b and HE2a. Red diamonds indicate CH_4 (gas-phase) match points; blue squares indicate volcanic match points between WD and GISP2 (ref. 27).

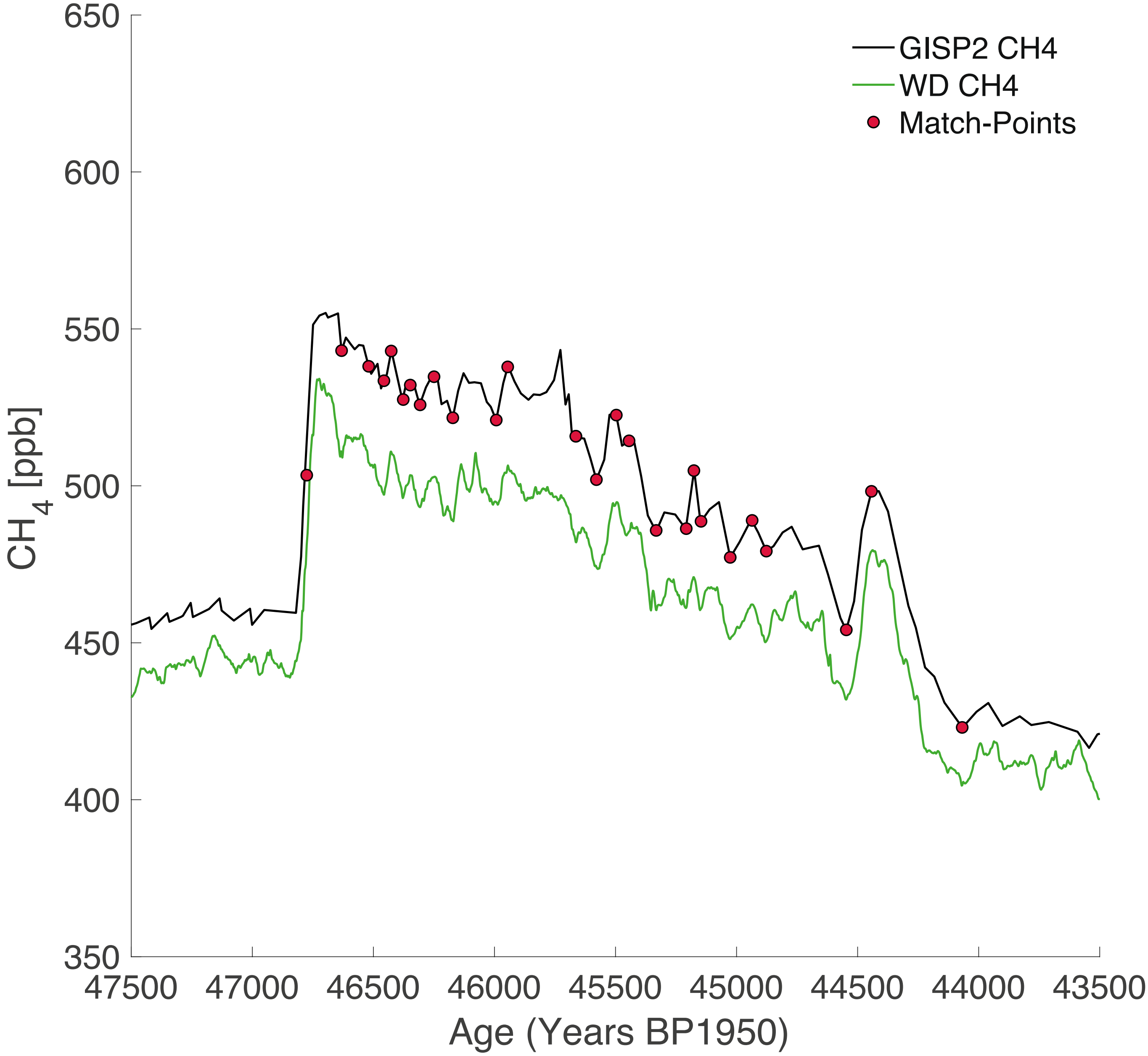

Extended Data Fig. 8 | Gas-phase synchronization of GISP2 and WD CH_4 records over DO12. CH_4 match-points (red circles) and GISP2 CH_4 record (black; this study), WD CH_4 record[17] (green). The use of an automated correlation scheme indicates that visual match-points are accurate to +/− 14 years.

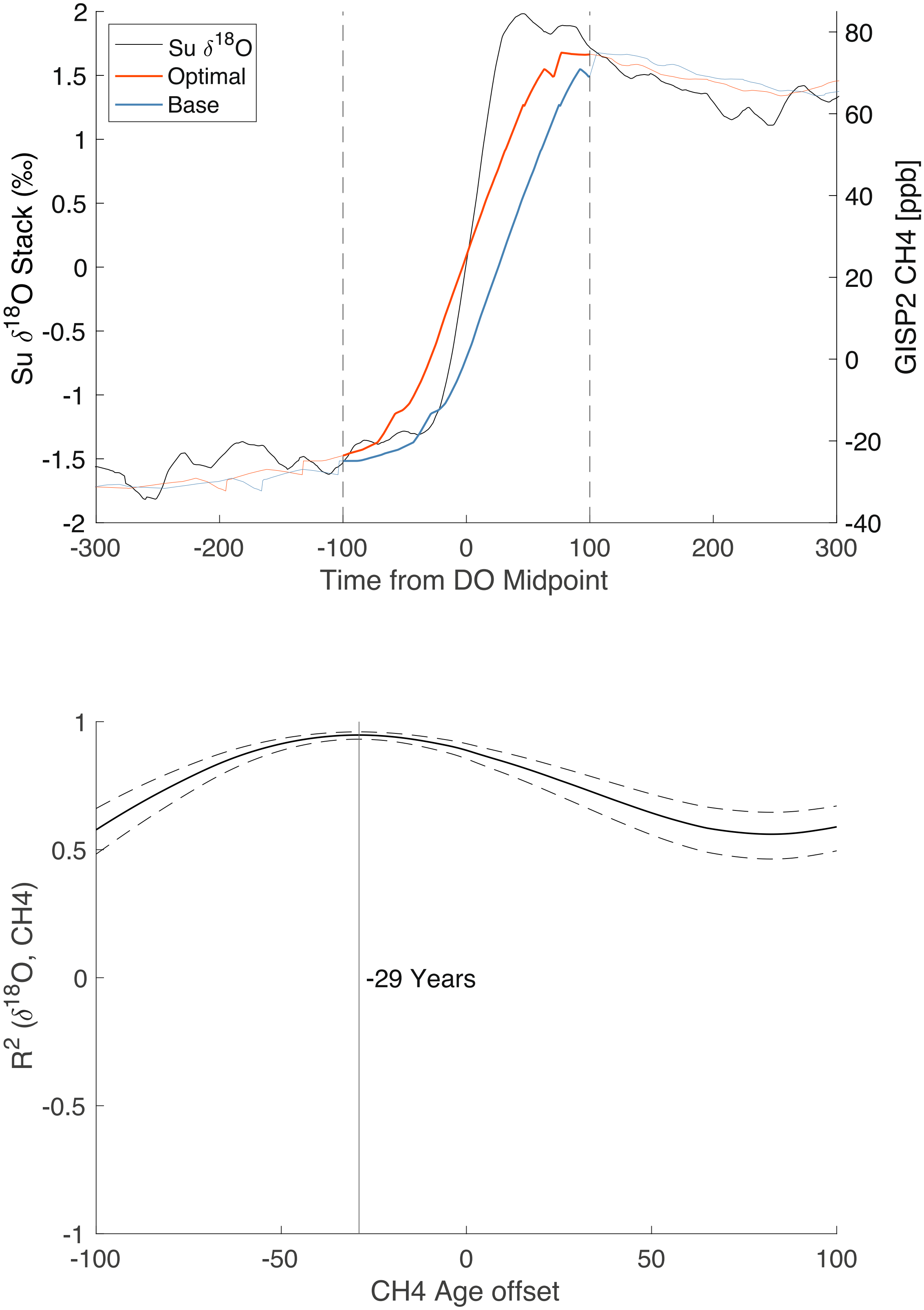

Extended Data Fig. 9 | Lead-Lag analysis of CH_4 and Greenland $\delta^{18}O$. Top panel: Summit (Su, average of GRIP and GISP2) $\delta^{18}O$ (black); GISP2 CH_4 stack, base record in blue and age-shifted record in red; Vertical dashed lines indicate correlation window. Bottom panel: squared correlation coefficient between GISP2 CH_4 and Su $\delta^{18}O$ for a range of age-offsets between records. Dashed lines indicate the 95% confidence level for correlations. Both records are the 25-year running average. Results are insensitive to changes in the window of correlation and the amount of smoothing.

Extended Data Table 1 | Heinrich Stadial (HS) and Heinrich Event (HE) timings used in this study

Feature	Source	GISP2 Depth (m)	BIC Age (yr bp1950)	GICC05 Age (yr bp1950)	WD2014 Age (yr bp1950)
HS1 termination	a	1797.21	14550.0	14628	14550.0
HE1	b	1853.40	16180	15904	16154
HS1 onset	c	1864.84	17850.6	17500	17850.6
HS2a termination	d	1986.96	23353.3	23340	23353.6
HE2a	b	2014.60	24090	24192	24057
HS2a onset	c	1999.18	24070.8	24120	24070.8
HS2b termination	c	2014.29	25018.0	25110	25017.5
HE2b	b	2038.60	25600	25877	25576
HS2b onset	c	2025.50	25827.5	25910	25827.5
HS3 termination	a	2076.29	28925.0	28838	28925.2
HE3	b	2107.60	30200	30054	30284
HS3 onset	a	2097.48	30574.3	30571	30563.6
HS4 termination	a	2232.02	38166.1	38165	38313.9
HE4	b	2257.90	39390	39426	39584
HS4 onset	a	2252.60	39905	39905	40049.2
HS5 termination	a	2358.79	46794.5	46794	46964.2
HE5	b	2379.60	48110	48139	48371
HS5 onset	a	2374.51	48440	48440	48584.3

HE timings are inferred by abrupt methane features hypothesized to be synchronous with HE. HE ages are at the midpoints of the CH_4 peaks with corresponding GISP2 depth of the gas-phase feature. Where HS timings are distinct from DO conditions, boundaries are based on Ca^{2+} concentrations in GISP2 (See Extended Data Fig. 1, Methods). Where the timing between HS and DO stadial is indistinct, previously published boundaries are provided. HS boundary depth is for ice-phase onset or termination features in the GISP2 ice core with corresponding ages. Sources for boundaries are as follows: a, previously published[24]. b, this study as the midpoint of GISP2 CH_4. c, this study utilizing Rampfit[52] on GISP2 Ca^{2+}. d, previously published[46].